iScience

CellPress
OPEN ACCESS

Article

Efficient Photoelectron Capture by Ni Decoration in *Methanosarcina barkeri*-CdS Biohybrids for Enhanced Photocatalytic CO_2-to-CH_4 Conversion

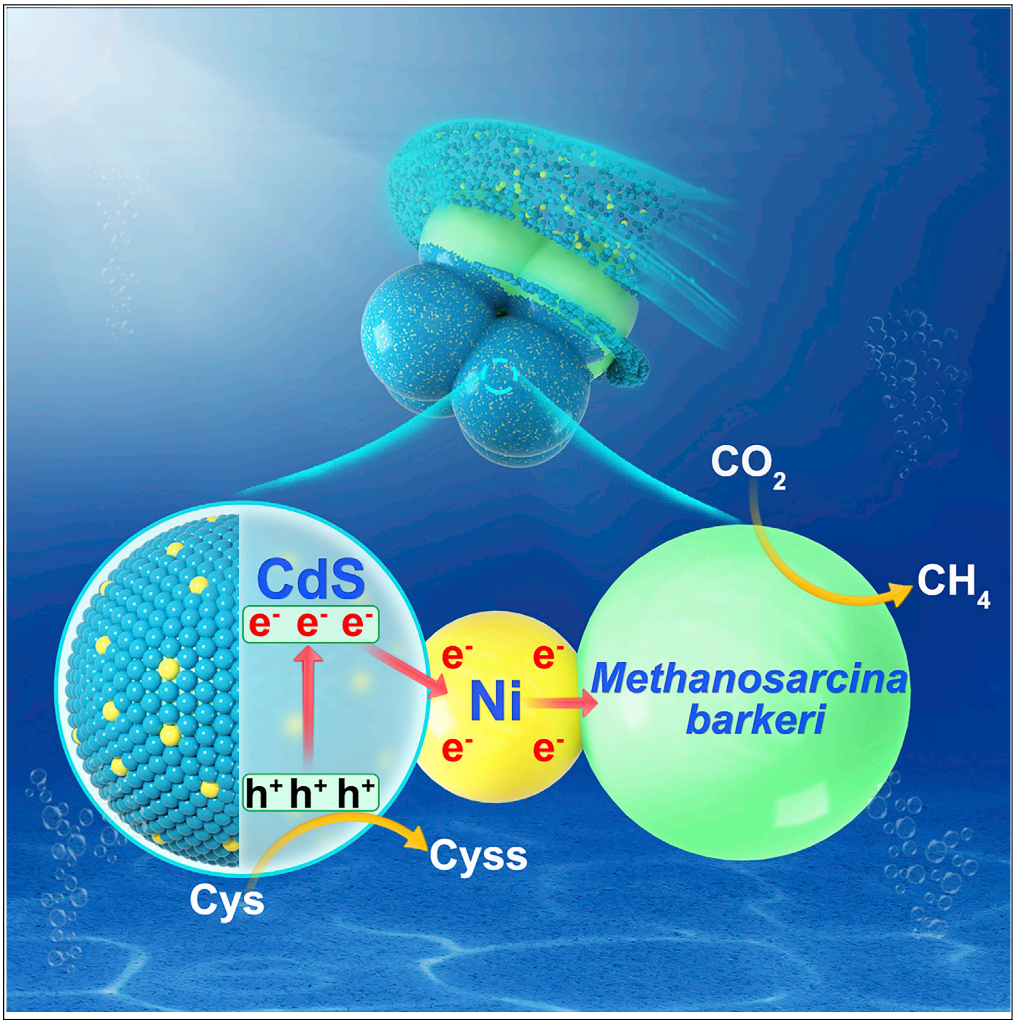

Jie Ye, Guoping Ren, Li Kang, Yiyun Zhang, Xing Liu, Shungui Zhou, Zhen He

sgzhou@soil.gd.cn

HIGHLIGHTS

M. barkeri-Ni:CdS biohybrids were successfully developed for CO_2 reduction

A highest *QE* of 2.08% was achieved by the *M. barkeri*-$Ni_{(0.75\%)}$:CdS biohybrids

Ni dopants effectively suppressed the electron-hole recombination in biohybrids

Ni doping changed the metabolic status of *M. barkeri* in biohybrids

Ye et al., iScience *23*, 101287
July 24, 2020 © 2020 The Author(s).
https://doi.org/10.1016/j.isci.2020.101287

iScience

CellPress
OPEN ACCESS

Article

Efficient Photoelectron Capture by Ni Decoration in *Methanosarcina barkeri*-CdS Biohybrids for Enhanced Photocatalytic CO_2-to-CH_4 Conversion

Jie Ye,[1] Guoping Ren,[1] Li Kang,[1] Yiyun Zhang,[1] Xing Liu,[1] Shungui Zhou,[1,3,*] and Zhen He[2]

SUMMARY

Semi-artificial photosynthesis (biohybrid) provides an intriguing opportunity for efficient CO_2-to-CH_4 conversion. However, creating a desirable semiconductor in biohybrids remains a great challenge. Here, by doping Ni into CdS nanoparticles, we have successfully developed the *Methanosarcina barkeri*-Ni:CdS biohybrids. The CH_4 yield by the *M. barkeri*-$Ni_{(0.75\%)}$:CdS biohybrids was approximately 250% higher than that by the *M. barkeri*-CdS biohybrids. The suitable Ni dopants serve as an effective electron sink, which accelerates the photoelectron transfer in biohybrids. In addition, Ni doping changes the metabolic status of *M. barkeri* and results in a higher expression of a series of proteins for electron transfer, energy conversion, and CO_2 fixation. These increased proteins can promote the photoelectron capture by *M. barkeri* and injection into cells, which trigger a higher intracellular reduction potential to drive the reduction of CO_2 to CH_4. Our discovery will offer a promising strategy for the optimization of biohybrids in the solar-to-chemical conversion.

INTRODUCTION

Solar-driven carbon dioxide (CO_2) reduction into high-value biofuels such as methane (CH_4) is a promising approach to alleviate both global energy challenge and greenhouse effect (Kim and Kwon, 2019). The traditional photocatalytic systems with various inorganic catalysts/enzymes are challenged by several critical drawbacks including poor CH_4/H_2 selectivity and lack of a self-replication ability (Nichols et al., 2015; Wagner et al., 2016). Semi-artificial photosynthesis (biohybrid), which synergistically combines the efficient light harvesting of semiconductors with the excellent biocatalytic capacity in methanogens, can provide a unique and intriguing opportunity for efficient CO_2-to-CH_4 conversion (Kornienko et al., 2018; Tremblay et al., 2020). The reducing equivalent [H] from photoelectrons in a semiconductor can be trapped by methanogens for metabolic activities via H_2ase-mediated and cytochrome-mediated pathways (Ye et al., 2019). To achieve excellent photocatalytic performance for practical applications, the desirable semiconductor in biohybrids should be developed to enhance the photoelectron separation, transfer, and capture.

Metal chalcogenides such as cadmium sulfide (CdS) semiconductors are excellent candidates of light harvesters in biohybrids due to their distinct characteristics such as tunable band gaps, rich surface binding sites, excellent extinction coefficients and favorable conduction/valence band energies (Zhukovskyi et al., 2015). A variety of efforts have been made to effectively suppress the rapid and severe recombination of photo-induced electrons and holes in CdS semiconductors (Wei et al., 2018). For example, integration with other semiconductors has created heterostructures such as CdS/ZnSe (Grennell et al., 2017), MoS_2/CdS (Yuan et al., 2018), and TiO_2/CdS (Luo et al., 2012; Park et al., 2016), whereas increasing the spatial overlap between electron-donating and electron-accepting semiconductors remains a challenge. Although the addition of molecular linkers, e.g., 4-mercaptobenzoic acid, was proved to be effectively improve the charge transfer process among different semiconductors (Dibbell et al., 2009), the formed organic ligands may be unfavorable for shuffling photoelectrons for surface catalytic sites (Hines and Kamat, 2013). The separation of photogenerated charge carriers can be addressed by depositing noble metals such as Pd (Wu et al., 2012), Pt (Jiang et al., 2015), and Au (Serra et al., 2015) on the surface of CdS as cocatalysts to restrain the recombination of electron-hole pairs. However, the scarcity and high cost of these noble metals trigger the development of an alternative and noble-metal-free system.

[1] Fujian Provincial Key Laboratory of Soil Environmental Health and Regulation, College of Resources and Environment, Fujian Agriculture and Forestry University, Fuzhou 350002, China

[2] Department of Energy, Environmental and Chemical Engineering, Washington University in St. Louis, St. Louis, MO 63130, USA

[3] Lead Contact

*Correspondence: sgzhou@soil.gd.cn

https://doi.org/10.1016/j.isci.2020.101287

Doping nickel (Ni) into CdS nanoparticles (Ni:CdS) has been proved to be a versatile approach to enhance the photocatalytic performance (Chai et al., 2016; Simon et al., 2014). The dopants are demonstrated to significantly improve the stability of CdS nanoparticles (Wang et al., 2018), because metal ions can interact with the CdS semiconductor to form a strong metal-sulfur binding in the lattice, which appears as an advantage over metal complex catalysts that effectively avoid the leaching of cations (Nag et al., 2012). In addition, Ni can serve as an effective electron outlet that promotes the migration of photoelectrons to the surface (Dong et al., 2015). Nevertheless, the excellent photocatalytic performance of Ni:CdS semiconductors, such as splitting alcohol into H_2 and CO_2 reduction with a high selectivity, was only demonstrated in the nonbiological systems (Wang et al., 2018). To our knowledge, little is known about the interaction between Ni:CdS semiconductors and microorganisms (methanogens). Particularly, the effect of the Ni-decorated semiconductor surface on the photoelectron transfer and capture by methanogens is unclear. Although the importance of Ni as an essential nutrient for methanogens was reported, such as the formation of Ni-Fe hydrogenases and cofactor F_{430} (Mulrooney and Hausinger, 2003), the metal toxicity on enzyme functions and structures may also inactivate methanogenic activity (Paulo et al., 2017). Therefore, it is of great interest to investigate the potential of Ni-decorated CdS to improve methanogenesis in biohybrids.

Methanosarcina barkeri was the methanogen that could participate in the direct interspecies electron transfer process (Rotaru et al., 2014), and its basic physiology and biochemistry was better understood than those of other methanogens (Kulkarni et al., 2018; Mand et al., 2018). Therefore, *M. barkeri* was selected to combine with Ni:CdS semiconductors to construct Ni-decorated *M. barkeri*-CdS (*M. barkeri*-Ni:CdS) biohybrids. The characterization of Ni:CdS semiconductors, such as the distribution, composition, and photoelectrochemical performance, was conducted. Importantly, the performance and mechanisms of *M. barkeri*-Ni:CdS biohybrids for methanogenesis were experimentally studied. This work was expected to offer a promising strategy to optimize biohybrids in the solar-to-chemical production.

RESULTS AND DISCUSSION

Characterization of *M. barkeri*-Ni:CdS Biohybrids

The Ni:CdS semiconductors were synthesized according to Wang et al. (2018), where the doped Ni atoms were efficiently embedded in CdS to capture photoelectrons at surface catalytic sites. When the growth of *M. barkeri* (DSM 800) reached an exponential phase (OD_{600}~0.2) in 50 mL anaerobic heterotrophic medium (Table S1), the successfully synthesized pure Ni:CdS semiconductors (Figures S1–S5) were added at a dosage of 0.6 mmol/L in a 100% N_2 atmosphere according to the preliminary results (Figure S6). Then the mixture was placed in the shaker at 37°C for 3 days to construct *M. barkeri*-Ni:CdS biohybrids. Because the highest CH_4 yield was achieved with an Ni weight ratio of 0.75% (Figure S7), the *M. barkeri*-$Ni_{(0.75\%)}$:CdS biohybrids were chosen as the main representative of *M. barkeri*-Ni:CdS biohybrids to do the characterization. To verify the presence of semiconductors in the biohybrids, we examined the fluorescence change *in vivo*. Under UV irradiation, bright yellow fluorescence (a typical color of metal chalcogenides) was observed in the *M. barkeri*-$Ni_{(0.75\%)}$:CdS biohybrids, whereas faint blue fluorescence was detected in the bare *M. barkeri*, which may be attributed to the cellular autofluorescence (Figure S8). Consistent results have been obtained by confocal laser scanning microscopic images, where bright yellow fluorescence well matched the shape of *M. barkeri* in the *M. barkeri*-$Ni_{(0.75\%)}$:CdS biohybrids (Figure 1A), but it was missed in the bare *M. barkeri* (Figure S8). The identity of the yellow fluorescence was ascertained by micro-Raman spectroscopy (Figures 1B and 1C). Like that in $Ni_{(0.75\%)}$:CdS semiconductors (Figure S1), a distinct peak at 300 cm^{-1} was detected in the *M. barkeri*-$Ni_{(0.75\%)}$:CdS biohybrids, which was identified as the distinct signal of Cd-S bond (Ma et al., 2015). All these results imply the presence of fluorescent Cd-S semiconductors that were combined with *M. barkeri* in the biohybrids.

We further confirmed the distribution and composition of Cd-S semiconductors in the biohybrids. Transmission electron microscopic (TEM) images reveal that the clusters of black dots with an average size of 10–100 nm were closely connected to the cell surface of *M. barkeri* (Figures 1D and 1E). The high angle annular dark field (HAADF) scanning transmission electron microscopic and energy-dispersive X-ray spectroscopic mapping images show that these particles were mainly composed of Cd, S, and Ni elements (Figures 1F–1I), which is further corroborated by the full scan survey X-ray photoelectron spectra. Specifically, identical to those in $Ni_{(0.75\%)}$:CdS semiconductors (Figure S3), the peaks of Cd $3d_{5/2}$ at 404.6 eV and Cd $3d_{3/2}$ at 411.4 eV in the *M. barkeri*-$Ni_{(0.75\%)}$:CdS biohybrids are associated with Cd^{2+} species, whereas the peaks of S $2p_{3/2}$ at 161.5 eV and S $2p_{1/2}$ at 162.8 eV are assigned to S^{2-} species (Yang et al., 2017). Importantly, four peaks for the chemical states of elemental Ni were demonstrated in the Ni 2p orbital spectrum (Figure S3),

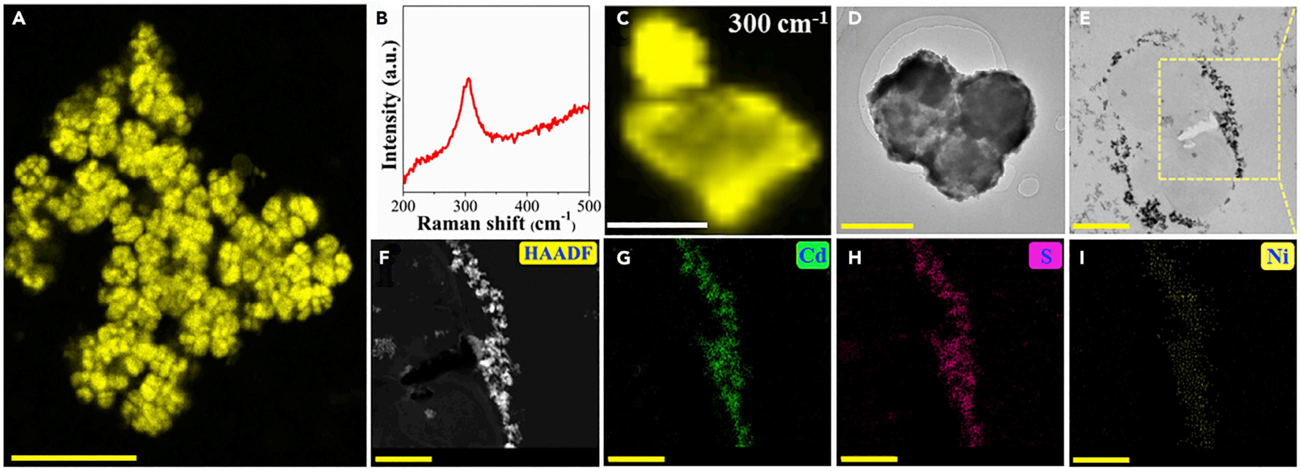

Figure 1. Characterization of the *M. barkeri*-$Ni_{(0.75\%)}$:CdS Biohybrids

Confocal laser scanning microscopic image (A); *in situ* Raman spectrum excited by a 532-nm laser (B); the Cd-S (at 300 cm^{-1}) single-cell Raman mapping (C); TEM images of the non-sectioned (D) and thin-sectioned *M. barkeri*-$Ni_{(0.75\%)}$:CdS biohybrids (E); high-angle annular dark-field image (F); and elements formed by Cd (G), S (H), and Ni (I) with energy-dispersive X-ray spectroscopic mapping. Scale bars: 20 μm in (A), 2 μm in (C and D), 1 μm in (E), and 0.5 μm in (F–I).

which was attributed to the Ni^{2+} state (Wang et al., 2018). In contrast, almost no nickel signal was detected on the X-ray photoelectron spectra of *M. barkeri*-CdS biohybrids (Figure S3), which demonstrates that nickel signal in the *M. barkeri*-$Ni_{(0.75\%)}$:CdS biohybrids was from $Ni_{(0.75\%)}$:CdS semiconductors. However, only CdS nanoparticles (PDF#75-0581) were identified with the X-ray diffraction (XRD) spectra and high-resolution TEM of $Ni_{(0.75\%)}$:CdS semiconductors and *M. barkeri*-$Ni_{(0.75\%)}$:CdS biohybrids. Three distinct diffraction peaks at 26.7°, 44.1°, and 52.2° were attributed to the (111), (220), and (311) crystal planes of CdS with d values of 0.35, 0.21, and 0.18 nm, respectively (Figures S4 and S5). There were no peaks for Ni nanocrystals or nickel compounds in XRD spectra, indicating that the low Ni doping amount did not significantly alter the cubic structure and crystallinity of CdS nanoparticles. This evidence suggests the successful decoration of Ni:CdS nanoparticles on the surface of *M. barkeri*.

Ni Doping Enhanced the Photocatalytic Performance of the Biohybrid

Photocatalytic CO_2-to-CH_4 conversion with the prepared biohybrids was performed at 35 ± 2°C under light irradiation. As shown in Figure 2A, only 6.13 ± 0.76 μmol CH_4 was obtained with the *M. barkeri*-CdS biohybrid, likely due to the lack of active sites and high recombination rate of electron-hole pairs. In contrast, Ni doping significantly enhanced the CH_4 yield to 21.50 ± 0.98 μmol with the *M. barkeri*-$Ni_{(0.75\%)}$:CdS biohybrid, which is ~250% higher than that with the *M. barkeri*-CdS biohybrids. The increase in CH_4 production in *M. barkeri*-$Ni_{(0.75\%)}$:CdS biohybrids was not caused by the addition of nickel alone, as almost no CH_4 was produced after the addition of an identical amount of Ni^{2+} for *M. barkeri* with or without light irradiation (Figure S9). However, further increasing Ni concentration in biohybrids (*M. barkeri*-$Ni_{(2.00\%)}$:CdS biohybrids) resulted in a lower CH_4 yield, which suggests that the doping should be optimized to achieve the desired performance. In addition, the role of different components in the *M. barkeri*-$Ni_{(0.75\%)}$:CdS biohybrids for CH_4 production was evaluated including *M. barkeri*, $Ni_{(0.75\%)}$:CdS, and light. Missing one of those factors led to negligible CH_4 production under these conditions (Figure 2B) and a significant decrease in protein contents (indication of biomass growth) (Figure 2C), which demonstrates the key roles of those factors in the CO_2-to-CH_4 conversion. The isotopic labeling experiments show that only the peaks of $^{13}CH_4$ (m/z = 17) and $^{13}CO_2$ (m/z = 45) were detected with ^{13}C-labeled $NaHCO_3$ as a carbon source (Figure 2D), which suggests that the produced CH_4 was derived from CO_2 reduction. The XRD and X-ray photoelectron spectra demonstrate the structural stability of $Ni_{(0.75\%)}$:CdS semiconductors in the biohybrids after 6 days of irradiation (Figures S3 and S4). However, the CH_4 production by *M. barkeri*-$Ni_{(0.75\%)}$:CdS biohybrids began to cease at day 4 (Figure 2A) with the decrease in biomass (Figure 2C). Due to sufficient CO_2 in the headspace (Figure 2D), the possible reason may be the quick depletion of only sacrificial hole scavenger cysteine, which causes the oxidative photodamage of cells. To further prove this speculation, a second injection of cysteine was conducted after 4 days of irradiation. The CH_4 production was enhanced with the addition of cysteine after the additional 5 days of irradiation (Figure S10).

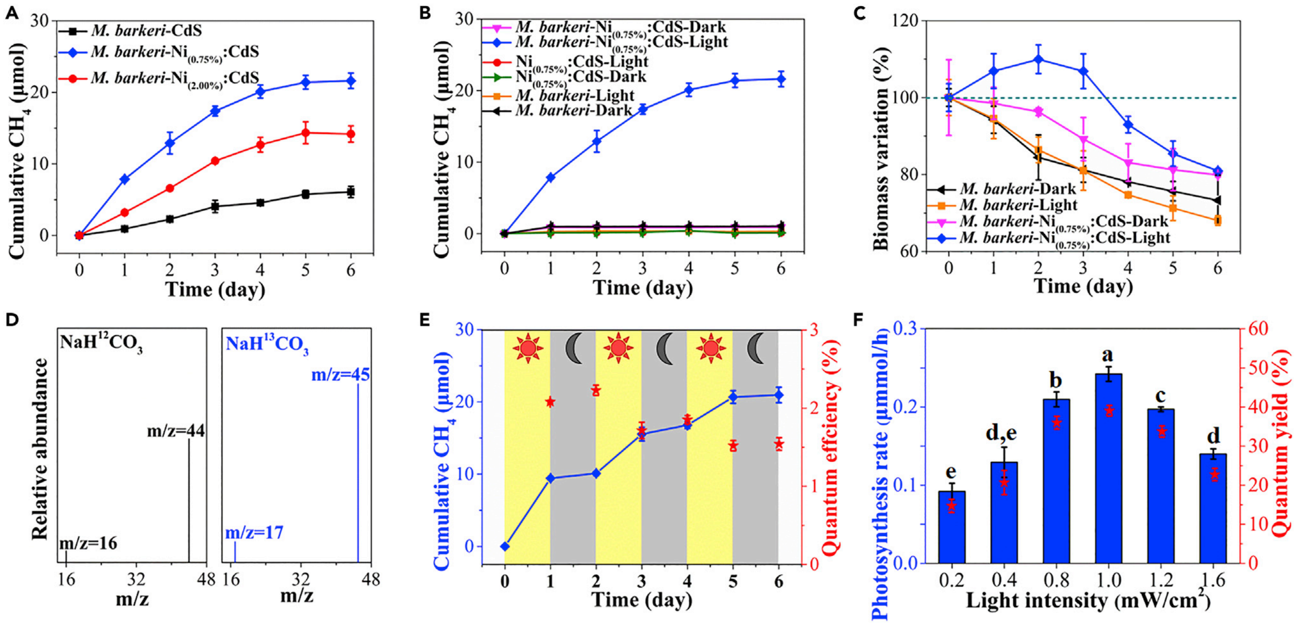

Figure 2. Photocatalytic Performance for CO_2-to-CH_4 Conversion with the Biohybrids

The CH_4 yields by biohybrids with various Ni doping amounts (A); photocatalytic CH_4 production by the *M. barkeri*-$Ni_{(0.75\%)}$:CdS biohybrids and deletional controls (B); biomass variation of natural *M. barkeri* and *M. barkeri*-$Ni_{(0.75\%)}$:CdS biohybrids (C); mass spectrometry of headspace gases with ^{12}C-labeled $NaHCO_3$ and ^{13}C-labeled $NaHCO_3$ as carbon sources in the media, respectively (D); photocatalytic CH_4 yields and quantum efficiencies (% incident light) of the *M. barkeri*-$Ni_{(0.75\%)}$:CdS biohybrids with a light-dark cycle of 1 day (E); photocatalytic CH_4 production rates and quantum yields based on the initial Cys concentration under different light intensities (F). Data are represented as mean ± SEM ($n = 3$), and the different letters represented statistically significant difference ($p < 0.05$) in different groups.

Therefore, the ceasing of CH_4 production in *M. barkeri*-$Ni_{(0.75\%)}$:CdS biohybrids can be attributed to the depletion of sacrificial hole scavenger cysteine.

The photocatalytic performance of the *M. barkeri*-$Ni_{(0.75\%)}$:CdS biohybrids was further evaluated with a light-dark cycle of 1 day (Figure 2E). The continuous increase in CH_4 concentration during several light-dark cycles suggests that the accumulated biosynthetic intermediates during the daytime can be used in the nighttime, which can effectively eliminate the catabolic energy loss that commonly occurs during the dark cycles in natural photosynthesis (Sakimoto et al., 2016; Larkum, 2010). A peak quantum efficiency of 2.08% ± 0.03% of total incident light was obtained with the *M. barkeri*-$Ni_{(0.75\%)}$:CdS biohybrid, which was significantly higher than those of *M. barkeri*-CdS and *M. barkeri*-$Ni_{(2.00\%)}$:CdS biohybrids (Figure S11). With the increase in light intensity, the CH_4 production rate followed a volcano-type trend (Figure 2F). The maximum CH_4 production rates with *M. barkeri*-$Ni_{(0.75\%)}$:CdS biohybrids reached 0.21 and 0.24 μmol/h with a light intensity of 0.8 and 1.0 mW/cm^2, respectively, which was higher than the reported CH_4 production rate of 0.19 μmol/h (Table S2), with a quantum yield of 21.60% ± 0.97% and 39.04% ± 1.34% (based on the initial Cys concentration, Supplemental Information). More importantly, the dosage of $Ni_{(0.75\%)}$:CdS semiconductor (0.6 mM) was lower than that in previous research (1.0 mM), which implies that better photocatalytic methanogenesis can be achieved by *M. barkeri*-$Ni_{(0.75\%)}$:CdS biohybrids with a lower semiconductor dose and lower light intensity. Afterward, the CH_4 production rate significantly decreased ($p < 0.05$), possibly related to the oxidative photodamage under high light intensities (Dumas et al., 2010) because photon energy under irradiation is the main driving force for the electron-hole separation in the *M. barkeri*-Ni(0.75%):CdS biohybrids. With the photon adsorption, the photoelectron (e^-) transition to conduction band was performed in the Ni(0.75%):CdS semiconductor. Then, the remaining holes (h^+) and consequently generated reactive oxygen species (ROS) such as hydrogen peroxide ($2H_2O + 2h^+ \rightarrow H_2O_2 + 2H^+$) and hydroxyl radical ($H_2O + h^+ \rightarrow \cdot OH + H^+$) (Nosaka and Nosaka, 2017) result in the oxidative stress for *M. barkeri* (Brioukhanov et al., 2000). At lower light intensity, sacrificial reagents Cys can effectively quench the photogenerated holes ($2Cys + 2h^+ \rightarrow Cyss + 2H^+$) (Sakimoto et al., 2016) and ROS (He and Häder, 2002), which protect *M. barkeri* against oxidative stress. In contrast, a too high light intensity will quickly increase the concentrations of h^+ and ROS, which become higher than the survival limit of

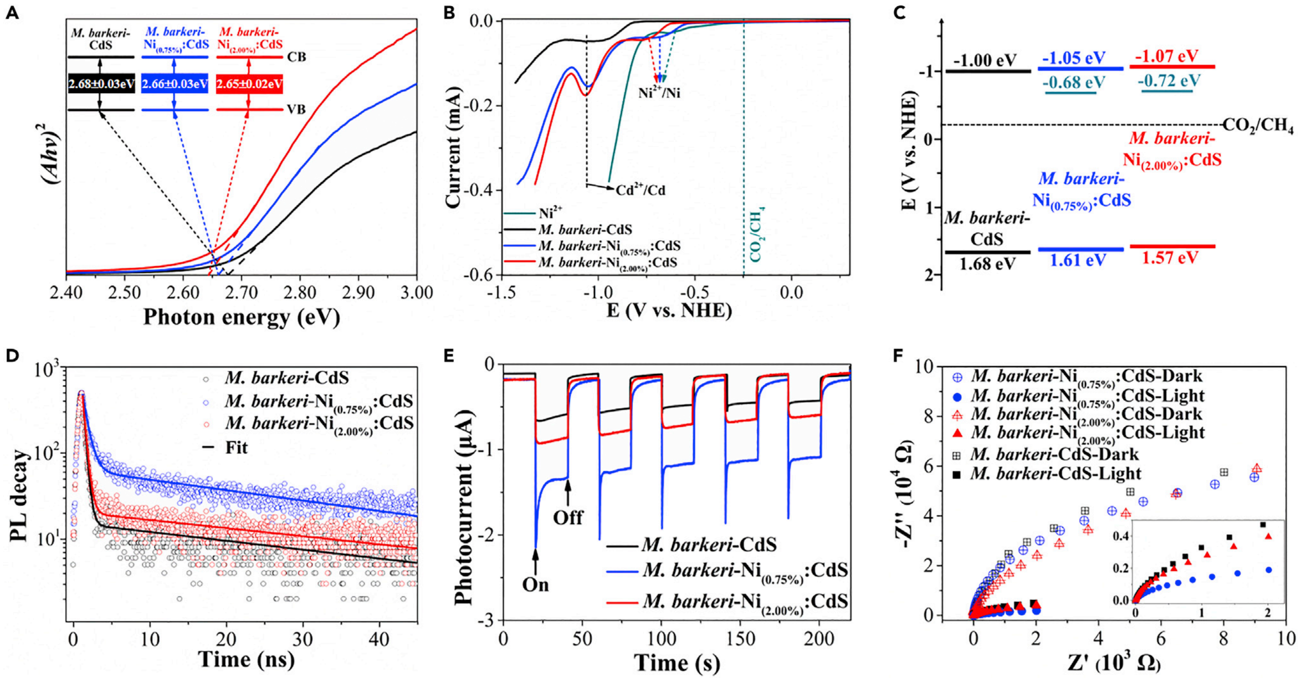

Figure 3. Photoelectrochemical Tests of the Biohybrids with Various Ni Doping Amounts

The band gaps of different biohybrids (A), linear sweep voltammetry curves of different biohybrids and free Ni^{2+} cations in water (B), energy band diagrams for different biohybrids (C), PL decay curves of different biohybrids (D), *I-t* curves under a light on/off cycle (20/20 s) (E), and Nyquist plots (F) with different biohybrids. Data are represented as mean ± SEM (n = 3).

M. barkeri (e.g., maximum 0.4 mM H_2O_2 stress, (Brioukhanov et al., 2006). A too high light intensity also causes the photocorrosion of the CdS semiconductor ($CdS + 2h^+ \rightarrow Cd^{2+} + S$, (Davis and Huang, 1991), which has a photoprotective role toward microorganisms. These results are consistent with the scanning electron microscopic images, where obvious cell shrinkage was observed in *M. barkeri*-Ni(0.75%):CdS biohybrids with light intensity of 1.6 mW/cm^2 (Figure S12).

Ni Doping Improved the Photoelectron Separation and Transfer Efficiency

To understand the intrinsic reason for the excellent performance of the Ni-decorated *M. barkeri*-CdS biohybrid, we evaluated the band structures of different semiconductors that governed the photoelectron separation and transfer. UV-visible (UV-vis) spectra show that the band gaps of CdS and $Ni_{(x)}$:CdS semiconductors in biohybrids were approximately 2.65–2.68 eV (Figure 3A), which were close to those of pure CdS and $Ni_{(x)}$:CdS semiconductors (2.64–2.67 eV, Figure S13). The values were larger than that of the bulk CdS (approximately 2.42 eV) (Thambidurai et al., 2011). The reason can be the small size of the synthesized semiconductor (<5 nm, see Figure S5), which caused the size-induced quantum confinement effect (Takagahara and Takeda, 1992). Similar results were reported in previous studies, wherein the band gap of CdS semiconductors reached 2.51–2.72 eV (Sakimoto et al., 2016; Brown et al., 2016; Chavhan et al., 2008). However, the observed absorption trailing below 2.60 eV in the UV-vis spectra suggests more doping defects in the *M. barkeri*-Ni:CdS biohybrids than in the *M. barkeri*-CdS biohybrids (Figure S14), which can promote the efficient charge transfer from inside to the surface of the semiconductors (Huang et al., 2017). In addition to the reduction peak of Cd^{2+}/Cd^0 at approximately −1.00 V versus normal hydrogen electrode (NHE) (Simon et al., 2014), one more peak at approximately −0.70 V versus NHE was detected in the *M. barkeri*-Ni:CdS biohybrids by linear sweep voltammetry (Figure 3B), which was assigned to the reduction of Ni^{2+}/Ni^0 (Han et al., 2012). Thus, the surface Ni could be used as efficient catalytic sites to capture photoelectrons for the CO_2 reduction. The cathodic photocurrents of *M. barkeri*-$Ni_{(x)}$:CdS biohybrids were higher than those of *M. barkeri*-CdS biohybrids, which indicates that the doping of Ni on CdS could further catalyze CO_2 reduction. The estimated energy bands of the *M. barkeri*-CdS and *M. barkeri*-Ni:CdS biohybrids are shown in Figure 3C. The upshift of the valence band (VB) after Ni doping was consistent with the analysis from the VB-X-ray photoelectron spectra (Figure S15), which may be beneficial for photoelectron transfer.

To further comprehend the variation of the band structure on the charge behavior of biohybrids, we evaluated the recombination rate of electron-hole pairs in the biohybrids by the steady-state photoluminescence (PL) spectra. The PL peaks approximately at 550 nm were found in all samples (Figure S16A) and became weaker at approximately 650 nm in the presence of methyl viologen (MV^{2+}), which sacrificed surface electrons (Figure S16B). The results indicate that the PL spectra mainly resulted from the radiative electron-hole recombination on the surface instead of in the bulk. Notably, the *M. barkeri*-$Ni_{(0.75\%)}$:CdS biohybrids showed a stronger surface photoemission than the *M. barkeri*-CdS biohybrid, which demonstrates the enhanced efficiencies of separation and capture of photoelectrons on the surface after Ni doping. However, increasing Ni concentration (*M. barkeri*-$Ni_{(2.00\%)}$:CdS biohybrid) decreased the PL peak intensity, which might be due to the nonradiative recombination of photoelectrons at bulk Ni sites. In addition, the time-resolved PL spectra show that the doped Ni (0.75 wt %) can serve as an effective electron sink on the surface to prolong the lifetime of photoinduced charge carriers by 213%, although an overly high Ni doping concentration can shorten the PL lifetime for surface radiative recombination (Figure 3D, Table S3). The results were corroborated by the amperometric *I-t* curves, where the *M. barkeri*-$Ni_{(0.75\%)}$:CdS biohybrids had higher photocurrent intensity than the *M. barkeri*-CdS and *M. barkeri*-$Ni_{(2.00\%)}$ biohybrids (Figure 3E). The Nyquist plot obtained from the *M. barkeri*-$Ni_{(0.75\%)}$:CdS biohybrids show a smaller arc radius than the *M. barkeri*-CdS and *M. barkeri*-$Ni_{(2.00\%)}$:CdS biohybrids with/without light irradiation, which confirms the enhanced electronic conductivity (Figure 3F). These results have illustrated that a suitable Ni doping amount can effectively accelerate the photoelectron transfer.

The density functional theory calculation was conducted to better understand the variation of the electronic band structure of semiconductors in the Ni-doped biohybrids. The doping models remained thermodynamically stable in theory with the relatively low change of total energy (1.10% and 2.21%) after structural relaxation (Figure S17). The lengths of Cd-S bonds in the Ni-doped semiconductors were slightly larger than those in bare CdS models (Figures 4A–4C), which might expand the crystal lattice (Huang et al., 2017). In addition, the Ni doping resulted in the increase of the valence band maximum (VBM) (Figure S18), which contributes to the narrower band gap of semiconductors in the *M. barkeri*-Ni:CdS biohybrids as shown in Figure 3A. Similar results were reported (Wu et al., 2011), where transition metal (Mn, Fe, and Ni) doping was proved to narrow the band gap of zinc blende CdS photocatalysts. We also calculated the density of states for Cd, S, and Ni orbitals. The conduction band minimum (CBM) and VBM in bare CdS are mainly composed of Cd 5s 4p and S 3p orbitals. However, after the substitution of Cd with Ni, more states of Ni 4s 4p were found in CBM states with the decreased contribution of Cd 5s 4p states (Figures 4D–4F). Thus, the photo-induced electrons preferred to migrate to Ni 4s 4p rather than Cd 5s 4p orbitals. In addition, higher electron transfer efficiencies were found in the electron density maps after Ni doping, which suggests the strong interaction between electron clouds of S and Ni atoms (Figures 4G–4I).

Ni Doping Promoted Electron Transfer from the Interface of Biohybrids to Cells

The isolation and analysis of membrane-bound proteins were conducted to evaluate the effect of Ni doping on electron transfer from the interface of biohybrids to microbial cells. It was found that no significant difference ($p > 0.05$) was observed between the concentrations of membrane-bound protein of different samples in the dark. In contrast, the concentrations of membrane-bound protein of *M. barkeri* were significantly increased after its interaction with semiconductors under light irradiation, with the highest value of 56.95 ± 0.25 mg/L with the *M. barkeri*-$Ni_{(0.75\%)}$:CdS biohybrids, which could be attributed to both an increase of cell number (based on the flow cytometry results) and an increase of membrane-bound protein per cell (based on the normalization results, Figure S19). In addition, higher concentrations of Ni and Cd elements were detected with the Ni-decorated biohybrids (Figure 5B). These results imply that suitable Ni doping improved the biocompatibility of CdS semiconductors with *M. barkeri*. To evaluate the activity of redox-active mediators that catalyzed the electron transport on the interface, square wave voltammetry measurement was performed (Figure 5C). Two dominant redox centers with a mid-potential of −0.21 V (versus standard hydrogen electrode) were detected, which could be assigned to cytochromes *b* (Kühn and Gottschalk, 1983). In addition, a higher catalytic current was obtained with the *M. barkeri*-Ni(0.75%):CdS biohybrids compared with *M. barkeri*-CdS and *M. barkeri*-Ni(2.00%):CdS biohybrids, which demonstrates more redox-active mediators in the membrane-bound protein layer. The increased amount of redox-active mediators at the interface of biohybrids after Ni doping

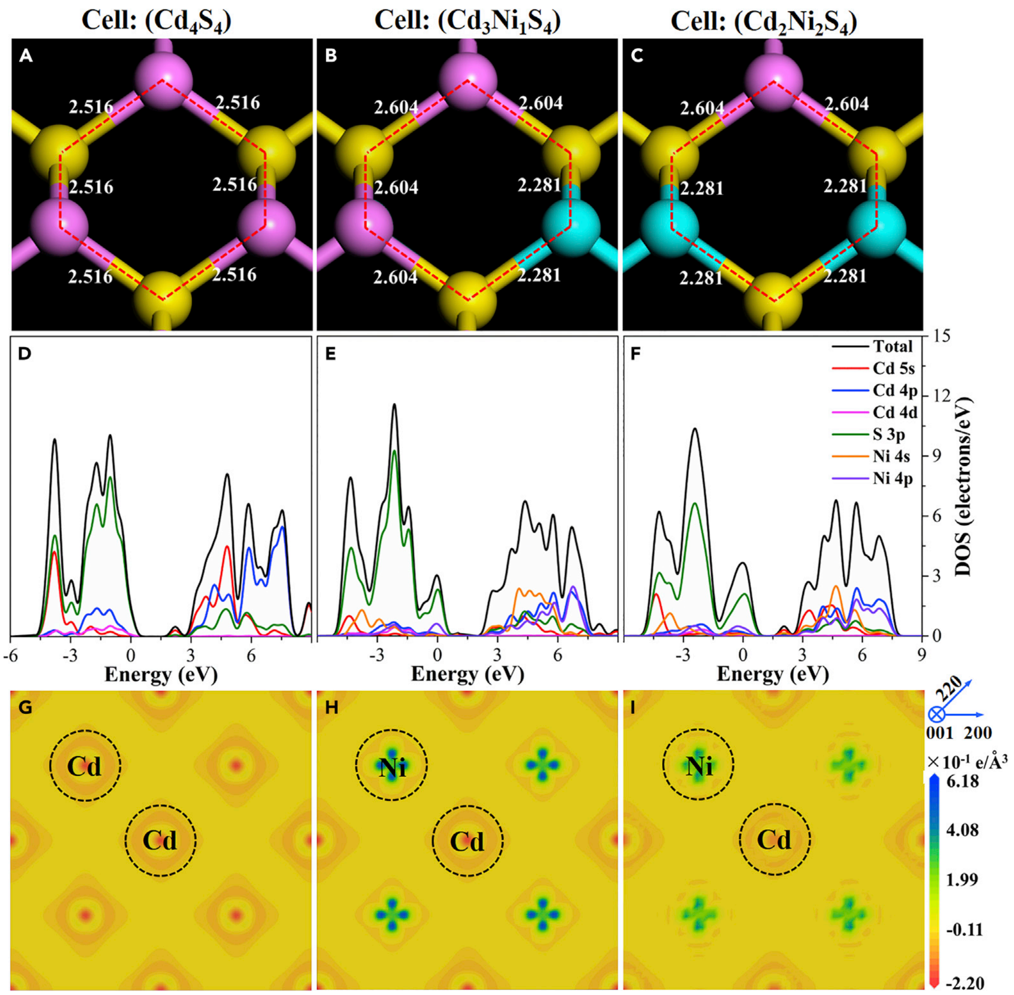

Figure 4. The Band Structure Evolution of CdS Semiconductors after Ni Doping

Calculated bond distances (A–C), densities of state (D–F), and electron density difference maps (G–I) of the simulated Ni-doped CdS systems with Cd_4S_4, $Cd_3Ni_1S_4$, and $Cd_2Ni_2S_4$.

effectively promoted the photoelectron capture by *M. barkeri* and generation of excessive intracellular reducing power under light irradiation (Figure 5D).

Proteins of *M. barkeri* in the *M. barkeri*-CdS and *M. barkeri*-$Ni_{(0.75\%)}$:CdS biohybrids were further analyzed by the untargeted proteomic technology. In total, 1,457 proteins were detected in both biohybrids. The principal-component analysis shows that two distinct groups in the score plots were observed (Figure 6A), which indicates that the Ni doping significantly influenced the physiological state of *M. barkeri* in biohybrids under light irradiation. Compared with the *M. barkeri*-CdS biohybrids, the number of proteins with significant upregulation (fold change >1.20 or $p < 0.05$) and downregulation (fold change <0.80 or $p < 0.05$) in the *M. barkeri*-$Ni_{(0.75\%)}$:CdS biohybrids reached 59 and 32, respectively (Figure 6B). The network analysis indicates that most of the 91 significantly changed proteins highly interacted with one another (Figure S20), which suggests that Ni doping led to systematic changes of the physiological status of *M. barkeri* such as electron transfer and energy conservation. A functional analysis of the significant proteins by the Clusters of Orthologous Groups (COG) database was further conducted (Figure 6C). In addition to energy production and conversion (C) and inorganic ion transport (P) proteins, other proteins with different functions were upregulated, including Cell-cycle-control/Cell-division/Chromosome-partitioning (D), Amino-acid-transport (E), Nucleotide-transport (F), Carbohydrate-transport (G), Coenzyme-transport (H), Translation/Ribosomal-structure/Biogenesis (J), Transcription (K), Replication/Recombination/Repair (L), Cell-wall/Membrane/Envelope-biogenesis (M), Posttranslational-modification/Protein-turnover/Chaperones

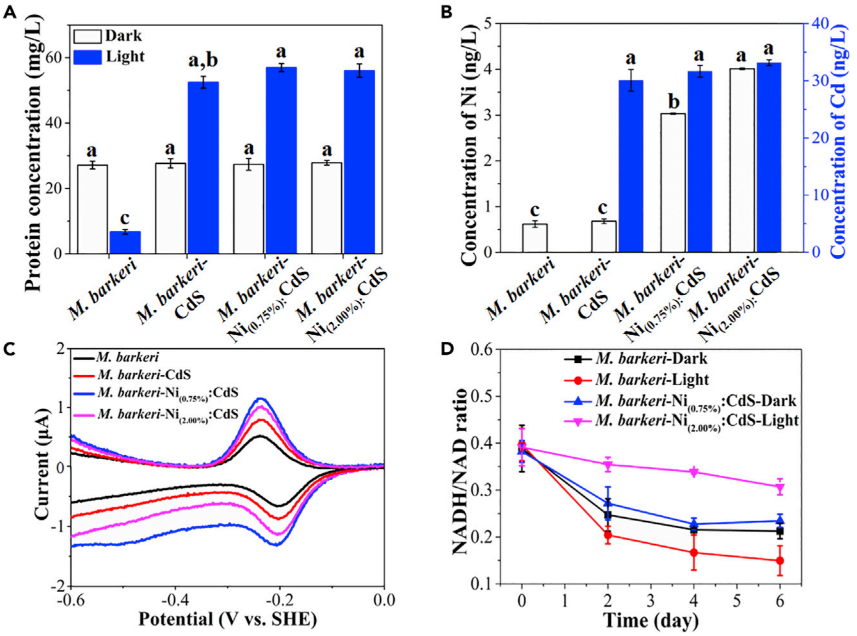

Figure 5. Characterization of the Membrane-Bound Protein and Activities of *M. barkeri* in Biohybrids with Various Ni Doping Amounts

Concentrations of membrane-bound protein (A), concentrations of Ni and Cd elements (B), square wave voltammetry curves of membrane-bound protein (C), and NADH/NAD ratio (D). Data are represented as mean ± SEM (n = 3), and the different letters represented statistically significant difference ($p < 0.05$) in different groups.

(O), Signal-transduction-mechanisms (T), Intracellular-trafficking/Secretion/Vesicular-transport (U), and Defense-mechanisms (V).

To better understand the mechanism, the proteins related to the charge transfer, carbon fixation, and energy conversion in *M. barkeri* were analyzed (Figures 7 and S21). Specifically, the carbon fixation during the CO_2-to-CH_4 conversion was catalyzed by different enzymes (Figure 8). Untargeted proteome data show that cytoplasmic formylmethanofuran dehydrogenase (Fmd) and methyl-S-CoM reductase (Mcr) were significantly upregulated in the *M. barkeri*-$Ni_{(0.75\%)}$:CdS biohybrids compared with *M. barkeri*-CdS biohybrids ($p < 0.05$). In addition, membrane-associated methyl-H_4SPT:CoM methyltransferase (Mtr), which can transmit methyl-tetrahydrosarcinapterin (CH_3-H_4SPT) into methyl-CoM (CH_3-CoM), was also significantly upregulated in the *M. barkeri*-$Ni_{(0.75\%)}$:CdS biohybrids. The membrane-associated proteins in *M. barkeri* also play an important role in the electron flow during methanogenesis, such as energy-converting [NiFe] hydrogenase (Ech, $H_2 + Fd_{ox} \rightleftharpoons Fd_{red}^{2-} + 2H^+$), methanophenazine-reducing [NiFe] hydrogenase (Vht, $H_2 + MP \rightleftharpoons MPH_2$), methanophenazine-dependent heterodisulphide reductase (Hdr, MPH_2 + CoM-S-S-CoB $\rightleftharpoons$ MP + HS-CoM + HS-CoB) (Thauer et al., 2008), and (Fpo, $MP + F_{420}H_2 \rightleftharpoons MPH_2 + F_{420}$) (Kulkarni et al., 2009). The significant upregulation ($p < 0.05$) of these enzymes in the *M. barkeri*-$Ni_{(0.75\%)}$:CdS biohybrid is beneficial for the photoelectron harvest and transfer. Simultaneously, the significant upregulation of NADH-dependent oxidoreductase (WP_011305330.1, WP_011307787.1), carbon-monoxide dehydrogenase (CODH), and ferredoxin (Fd) indicate that the harvested photoelectrons can trigger the increase of reducing equivalents and accelerate *in vivo* reductive reactions in the cells (Zhang et al., 2020). In addition, Ni was demonstrated to act as cofactors for many enzymes (Paulo et al., 2015). The significant upregulation of nickel transport proteins (*CbiN* and *CbiM*, $p < 0.05$) in the *M. barkeri*-$Ni_{(0.75\%)}$:CdS biohybrids and the increased membrane-associated ATP synthase (ATPase, $p < 0.05$) may stimulate the growth and metabolism of *M. barkeri*. Importantly, P-II family nitrogen regulator protein (WP_011307315.1) and ankyrin repeat domain-containing protein (WP_011307347.1), which functioned in signal transduction mechanisms, were significantly upregulated. ABC transporter ATP-binding proteins (WP_011305631.1, WP_048102540.1, WP_011305876.1), which are responsible for the defense mechanisms, were also

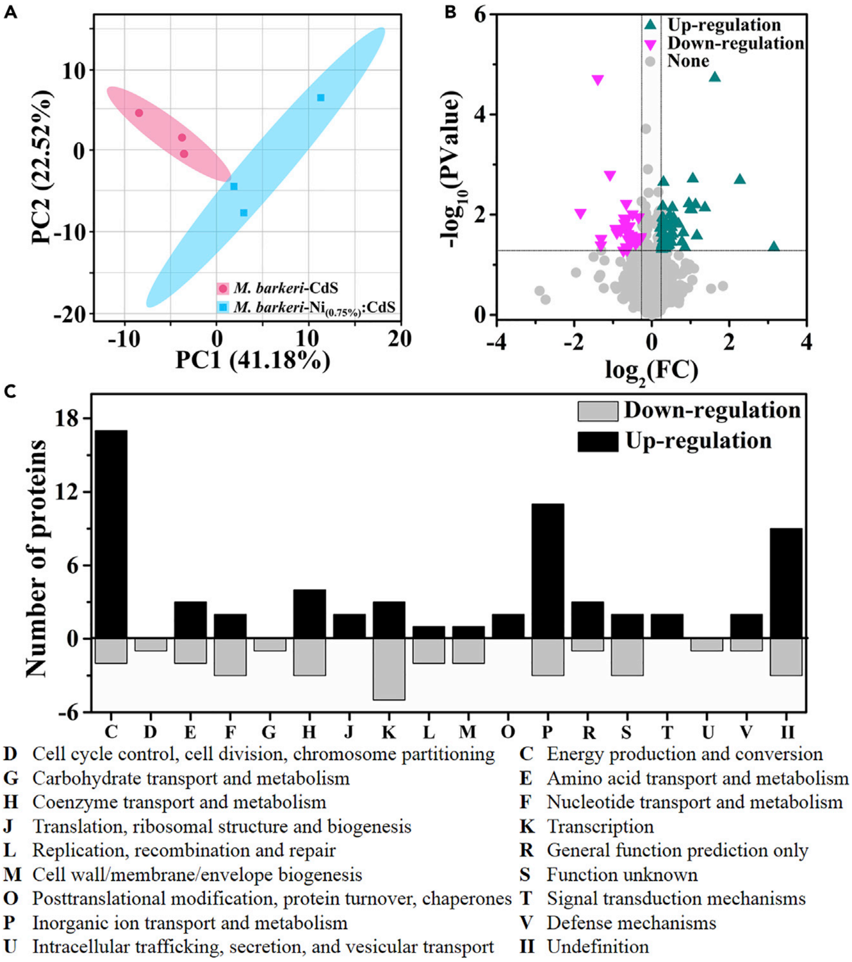

Figure 6. Assessment of Ni-Induced Physiological Perturbation of *M. barkeri*

Score plots (A) and volcano plots (B) of the proteome of *M. barkeri*-$Ni_{(0.75\%)}$:CdS biohybrids compared with *M. barkeri*-CdS biohybrids; COG functional annotation for the 91 proteins with significant variations in *M. barkeri*-$Ni_{(0.75\%)}$:CdS biohybrids compared with *M. barkeri*-CdS biohybrids (C).

significantly increased. These results indicate that *M. barkeri* adjusted the expression of related proteins to strengthen the stress resistance caused by Ni dopants.

Based on these results, a mechanism was proposed for the enhanced methanogenesis with the *M. barkeri*-Ni:CdS biohybrids (Figure 8). Ni:CdS semiconductors are decorated on the surface of *M. barkeri* and generate sufficient electrons under light irradiation. The photo-induced electrons migrate to Ni sites, which serve as an effective electron sink with Cys as a sacrificial reducing agent. In addition, Ni doping changes the metabolic status of *M. barkeri* and increases the concentration of proteins for electron transfer, energy conversion, and CO_2 fixation. With these proteins, the photoelectrons on the interface of biohybrids can be more easily injected into cells to generate excessive intracellular reducing power, which enhances the CO_2-to-CH_4 conversion.

Limitations of the Study

A comprehensive study of the energy conversion pathways and intermediate metabolites of *M. barkeri*-Ni:CdS biohybrids should be further conducted. In addition, the reason for different responses of various subunits (operons) of the proteins in *M. barkeri* after Ni doping must be explored. This information is beneficial for better understanding and constructing the biohybrid system.

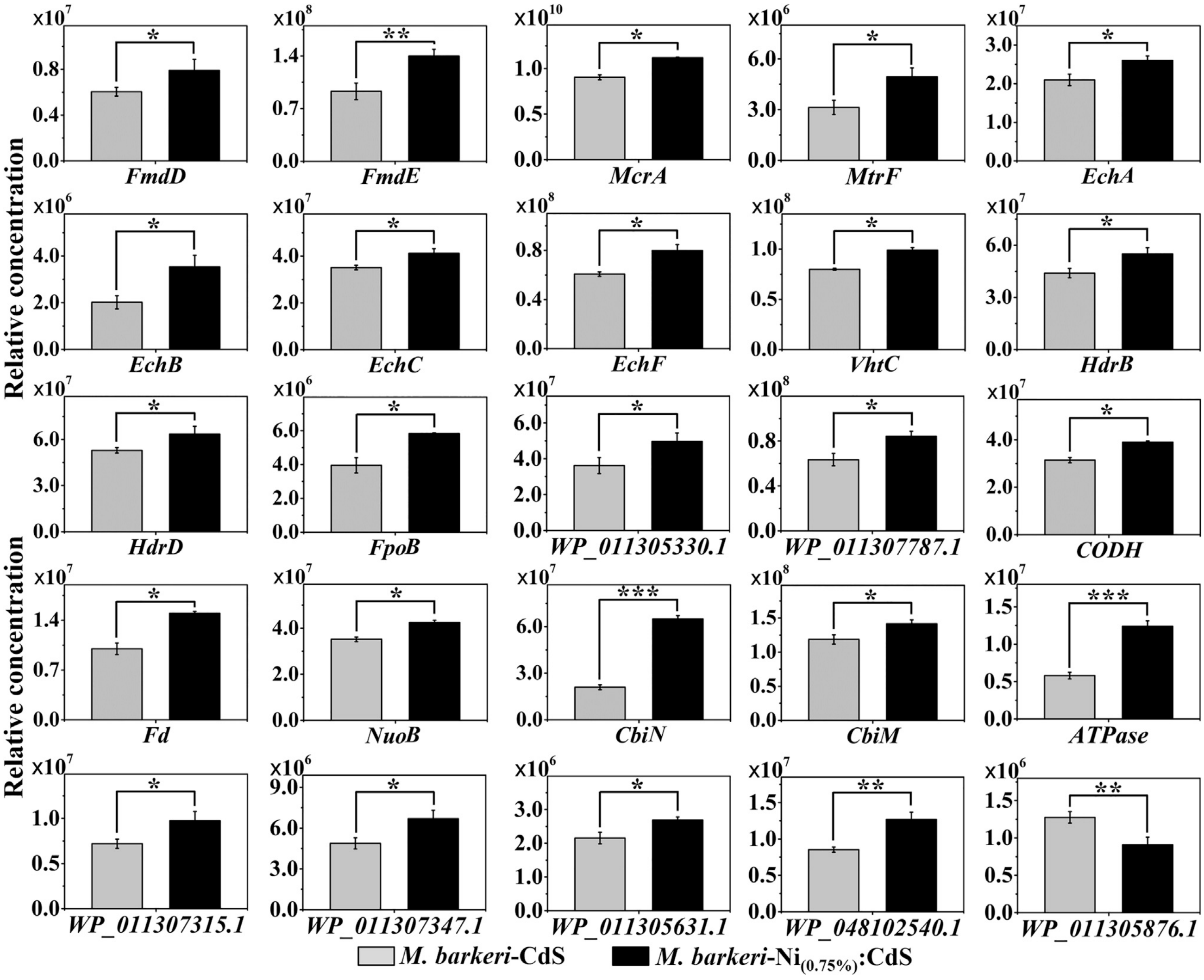

Figure 7. Relative Concentration of Proteins for Electron Transfer, Energy Conversion, and CO$_2$ Fixation in *M. barkeri*-Ni$_{(0.75\%)}$:CdS Biohybrids Compared with *M. barkeri*-CdS Biohybrids

Data are represented as mean ± SEM (n = 3). $^*p < 0.05$, $^{**}p < 0.01$, $^{***}p < 0.001$.

Resource Availability

Lead Contact

Further information and requests for resources and reagents should be directed to and will be fulfilled by the Lead Contact, Shungui Zhou (sgzhou@soil.gd.cn).

Materials Availability

Any materials generated and used in this study are available for dissemination to others.

Data and Code Availability

This study did not generate a new code. All relevant data are available from the Lead Contact upon reasonable request.

METHODS

All methods can be found in the accompanying Transparent Methods supplemental file.

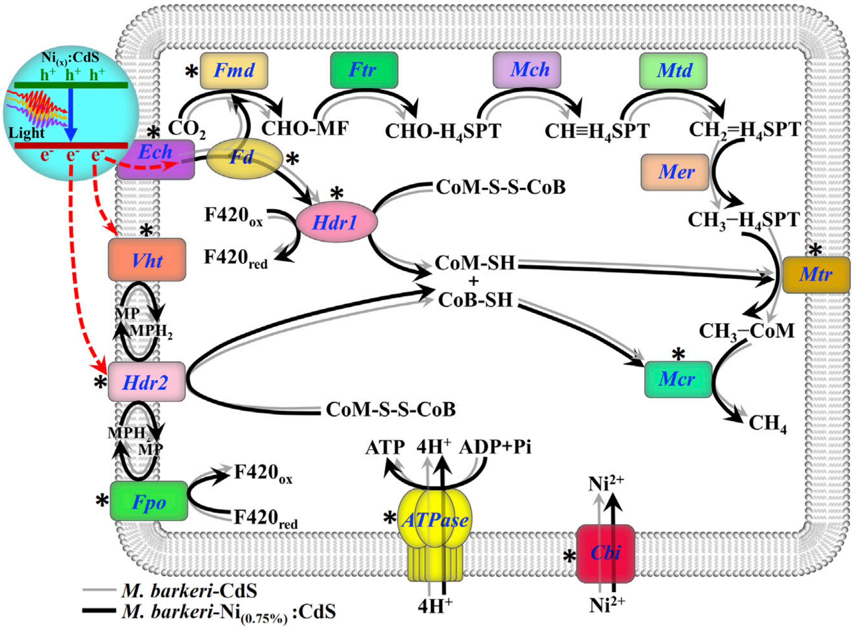

Figure 8. Pathways of Electron Transfer and CO_2 Reduction in *M. barkeri*-$Ni_{(0.75\%)}$:CdS Biohybrids and the Control

The degree of thickness of line (black and gray) represents the abilities of electron transfer and energy conversion.

*$p < 0.05$.

SUPPLEMENTAL INFORMATION

Supplemental Information can be found online at https://doi.org/10.1016/j.isci.2020.101287.

ACKNOWLEDGMENTS

This work was supported by the National Natural Science Foundation of China (41925028, 41977281), the Project of Fujian Provincial Department of Science and Technology of China (2018J01748), the Fujian Agriculture and Forestry University Program for Distinguished Young Scholar (XJQ2017003), the Project of the Fuzhou Municipal Department of Science and Technology of China (No. 2019-G-32), and US National Science Foundation (1603190).

AUTHOR CONTRIBUTIONS

J.Y. contributed to the experiments' designing and main manuscript writing; G.R. conducted the main experiments; L.K., Y.Z., and X.L. contributed to part of experiments; Z.H. and S.Z. helped to revise this manuscript. S.Z. contributed to the main funding acquisition. All authors reviewed and approved the final manuscript.

DECLARATION OF INTERESTS

The authors declare no competing interests.

Received: March 2, 2020
Revised: May 19, 2020
Accepted: June 13, 2020
Published: July 24, 2020

REFERENCES

Brioukhanov, A.L., Netrusov, A.I., and Eggen, R.I. (2006). The catalase and superoxide dismutase genes are transcriptionally up-regulated upon oxidative stress in the strictly anaerobic archaeon *Methanosarcina barkeri*. Microbiol. *152*, 1671–1677.

Brioukhanov, A., Netrusov, A., Sordel, M., Thauer, R.K., and Shima, S. (2000). Protection of *Methanosarcina barkeri* against oxidative stress: identification and characterization of an iron superoxide dismutase. Arch. Microbiol. *174*, 213–216.

Brown, K.A., Harris, D.F., Wilker, M.B., Rasmussen, A., Khadka, N., Hamby, H., Keable, S., Dukovic, G., Peters, J.W., Seefeldt, L.C., and King, P.W. (2016). Light-driven dinitrogen reduction catalyzed by a CdS: nitrogenase MoFe protein biohybrid. Science *352*, 448–450.

Chai, Z.G., Zeng, T.T., Li, Q., Lu, L.Q., Xiao, W.J., and Xu, D.S. (2016). Efficient visible light-driven splitting of alcohols into hydrogen and corresponding carbonyl compounds over a Ni-modified CdS photocatalyst. J. Am. Chem. Soc. *138*, 10128–10131.

Chavhan, S.D., Senthilarasu, S., and Lee, S.H. (2008). Annealing effect on the structural and optical properties of a $Cd_{1-x}Zn_xS$ thin film for photovoltaic applications. Appl. Surf. Sci. *254*, 4539–4545.

Davis, A.P., and Huang, C.P. (1991). The photocatalytic oxidation of sulfur-containing organic compounds using cadmium sulfide and the effect on CdS photocorrosion. Water Res. *25*, 1273–1278.

Dibbell, R.S., Youker, D.G., and Watson, D.F. (2009). Excited-state electron transfer from CdS quantum dots to TiO_2 nanoparticles via molecular linkers with phenylene bridges. J. Phys. Chem. C *113*, 18643–18651.

Dong, Y.T., Choi, J.L., Jeong, H.K., and Son, D.H. (2015). Hot electrons generated from doped quantum dots via upconversion of excitons to hot charge carriers for enhanced photocatalysis. J. Am. Chem. Soc. *137*, 5549–5554.

Dumas, E., Gao, C., Suffern, D., Bradforth, S.E., Dimitrijevic, N.M., and Nadeau, J.L. (2010). Interfacial charge transfer between CdTe quantum dots and gram negative vs gram positive bacteria. Environ. Sci. Technol. *44*, 1464–1470.

Grennell, A.N., Utterback, J.K., Pearce, O.M., Wilker, M.B., and Dukovic, G. (2017). Relationships between exciton dissociation and slow recombination within ZnSe/CdS and CdSe/CdS dot-in-rod heterostructures. Nano Lett. *17*, 3764–3774.

Han, Z.J., Qiu, F., Eisenberg, R., Holland, P.L., and Krauss, T.D. (2012). Robust photogeneration of H_2 in water using semiconductor nanocrystals and a nickel catalyst. Science *338*, 1321–1324.

He, Y.Y., and Häder, D.P. (2002). UV-B-induced formation of reactive oxygen species and oxidative damage of the cyanobacterium *Anabaena* sp.: protective effects of ascorbic acid and N-acetyl-L-cysteine. J. Photoch. Photobiol. B *66*, 115–124.

Hines, D.A., and Kamat, P.V. (2013). Quantum dot surface chemistry: ligand effects and electron transfer reactions. J. Phys. Chem. C *117*, 14418–14426.

Huang, H.M., Dai, B.Y., Wang, W., Lu, C.H., Kou, J.H., Ni, Y.R., Wang, L.Z., and Xu, Z.Z. (2017). Oriented built-in electric field introduced by surface gradient diffusion doping for enhanced photocatalytic H_2 evolution in CdS nanorods. Nano Lett. *17*, 3803–3808.

Jiang, X.L., Fu, X.L., Zhang, L., Meng, S.G., and Chen, S.F. (2015). Photocatalytic reforming of glycerol for H_2 evolution on Pt/TiO_2: fundamental understanding the effect of co-catalyst Pt and the Pt deposition route. J. Mater. Chem. A *3*, 2271–2282.

Kim, J., and Kwon, E.E. (2019). Photoconversion of carbon dioxide into fuels using semiconductors. J. CO_2 Util. *33*, 72–82.

Kornienko, N., Zhang, J.Z., Sakimoto, K.K., Yang, P., and Reisner, E. (2018). Interfacing nature's catalytic machinery with synthetic materials for semi-artificial photosynthesis. Nat. Nanotechnol. *13*, 890–899.

Kühn, W., and Gottschalk, G. (1983). Characterization of the cytochromes occurring in *Methanosarcina* species. Eur. J. Biochem. *135*, 89–94.

Kulkarni, G., Kridelbaugh, D.M., Guss, A.M., and Metcalf, W.W. (2009). Hydrogen is a preferred intermediate in the energy-conserving electron transport chain of *Methanosarcina barkeri*. Proc. Natl. Acad. Sci. U S A *106*, 15915–15920.

Kulkarni, G., Mand, T.D., and Metcalf, W.W. (2018). Energy conservation via hydrogen cycling in the methanogenic archaeon *Methanosarcina barkeri*. MBio *9*, e01256-18.

Larkum, A.W.D. (2010). Limitations and prospects of natural photosynthesis for bioenergy production. Curr. Opin. Biotech. *21*, 271–276.

Luo, J.S., Ma, L., He, T.C., Ng, C.F., Wang, S.J., Sun, H.D., and Fan, H.J. (2012). TiO_2/(CdS, CdSe, CdSeS) nanorod heterostructures and photoelectrochemical properties. J. Phys. Chem. C *116*, 11956–11963.

Ma, L.J., Liu, M.C., Jing, D.W., and Guo, L.J. (2015). Photocatalytic hydrogen production over CdS: effects of reaction atmosphere studied by in situ Raman spectroscopy. J. Mater. Chem. A *3*, 5701–5707.

Mand, T.D., Kulkarni, G., and Metcalf, W.W. (2018). Genetic, biochemical, and molecular characterization of *Methanosarcina barkeri* mutants lacking three distinct classes of hydrogenase. J. Bacteriol. *200*, e00342-18.

Mulrooney, S.B., and Hausinger, R.P. (2003). Nickel uptake and utilization by microorganisms. FEMS Microb. Rev. *27*, 239–261.

Nag, A., Chung, D.S., Dolzhnikov, D.S., Dimitrijevic, N.M., Chattopadhyay, S., Shibata, T., and Talapin, D.V. (2012). Effect of metal ions on photoluminescence, charge transport, magnetic and catalytic properties of all-inorganic colloidal nanocrystals and nanocrystal solids. J. Am. Chem. Soc. *134*, 13604–13615.

Nichols, E.M., Gallagher, J.J., Liu, C., Su, Y., Resasco, J., Yu, Y., Sun, Y., Yang, P., and Chang, C.J. (2015). Hybrid bioinorganic approach to solar-to-chemical conversion. Proc. Natl. Acad. Sci. U S A *112*, 11461–11466.

Nosaka, Y., and Nosaka, A.Y. (2017). Generation and detection of reactive oxygen species in photocatalysis. Chem. Rev. *117*, 11302–11336.

Park, H., Ou, H.H., Kang, U., Choi, J., and Hoffmann, M.R. (2016). Photocatalytic conversion of carbon dioxide to methane on TiO_2/CdS in aqueous isopropanol solution. Catal. Today *266*, 153–159.

Paulo, L.M., Ramiro-Garcia, J., van Mourik, S., Stams, A.J., and Sousa, D.Z. (2017). Effect of nickel and cobalt on methanogenic enrichment cultures and role of biogenic sulfide in metal toxicity attenuation. Front. Microbiol. *8*, 1341.

Paulo, L.M., Stams, A.J., and Sousa, D.Z. (2015). Methanogens, sulphate and heavy metals: a complex system. Rev. Environ. Sci. Bio. *14*, 537–553.

Rotaru, A.E., Shrestha, P.M., Liu, F., Shrestha, M., Shrestha, D., Embree, M., Zengler, K., Wardman, C., Nevin, K.P., and Lovley, D.R. (2014). A new model for electron flow during anaerobic digestion: direct interspecies electron transfer to *Methanosaeta* for the reduction of carbon dioxide to methane. Energ. Environ. Sci. *7*, 408–415.

Sakimoto, K.K., Wong, A.B., and Yang, P. (2016). Self-photosensitization of nonphotosynthetic bacteria for solar-to-chemical production. Science *351*, 74–77.

Serra, M., Albero, J., and García, H. (2015). Photocatalytic activity of Au/TiO_2 photocatalysts for H_2 evolution: role of the Au nanoparticles as a function of the irradiation wavelength. ChemPhysChem *16*, 1842–1845.

Simon, T., Bouchonville, N., Berr, M.J., Vaneski, A., Adrović, A., Volbers, D., Wyrwich, R., Döblinger, M., Susha, A.S., Rogach, A.L., et al. (2014). Redox shuttle mechanism enhances photocatalytic H_2 generation on Ni-decorated CdS nanorods. Nat. Mater. *13*, 1013.

Takagahara, T., and Takeda, K. (1992). Theory of the quantum confinement effect on excitons in quantum dots of indirect-gap materials. Phys. Rev. B *46*, 15578.

Thambidurai, M., Muthukumarasamy, N., Agilan, S., Arul, N.S., Murugan, N., and Balasundaraprabhu, R. (2011). Structural and optical characterization of Ni-doped CdS quantum dots. J. Mater. Sci. *46*, 3200–3206.

Thauer, R.K., Kaster, A.K., Seedorf, H., Buckel, W., and Hedderich, R. (2008). Methanogenic archaea: ecologically relevant differences in energy conservation. Nat. Rev. Microbiol. *6*, 579–591.

Tremblay, P.L., Xu, M., Chen, Y., and Zhang, T. (2020). Nonmetallic abiotic-biological hybrid photocatalyst for visible water splitting and carbon dioxide reduction. Iscience *23*, 100784.

Wagner, T., Ermler, U., and Shima, S. (2016). The methanogenic CO_2 reducing-and-fixing enzyme is bifunctional and contains 46 [4Fe-4S] clusters. Science *354*, 114–117.

Wang, J., Xia, T., Wang, L., Zheng, X.S., Qi, Z.M., Gao, C., Zhu, J.F., Li, Z.Q., Xu, H.X., and Xiong, Y.J. (2018). Enabling visible-light-driven selective CO_2 reduction by doping quantum dots: Trapping electrons and suppressing H_2 evolution. Angew. Chem. Int. Ed. *57*, 16447–16451.

Wei, R.B., Huang, Z.L., Gu, G.H., Wang, Z., Zeng, L., Chen, Y., and Liu, Z.Q. (2018). Dual-cocatalysts decorated rimous CdS spheres advancing highly-efficient visible-light photocatalytic hydrogen production. Appl. Catal. B Environ. *231*, 101–107.

Wu, J.C., Zheng, J., Wu, P., and Xu, R. (2011). Study of native defects and transition-metal (Mn, Fe, Co, and Ni) doping in a zinc-blende CdS photocatalyst by DFT and hybrid DFT calculations. J. Phys. Chem. C *115*, 5675–5682.

Wu, X., Song, Q., Jia, L., Li, Q., Yang, C., and Lin, L. (2012). Pd-Gardenia-TiO_2 as a photocatalyst for H_2 evolution from pure water. Int. J. Hydrogen Energ. *37*, 109–114.

Yang, H., Jin, Z., Fan, K., Liu, D., and Lu, G. (2017). The roles of Ni nanoparticles over CdS nanorods for improved photocatalytic stability and activity. Superlattice. Microst. *111*, 687–695.

Ye, J., Yu, J., Zhang, Y.Y., Chen, M., Liu, X., Zhou, S., and He, Z. (2019). Light-driven carbon dioxide reduction to methane by *Methanosarcina barkeri*-CdS biohybrid. Appl. Catal. B Environ. *257*, 117916.

Yuan, Y.J., Li, Z.J., Wu, S.T., Chen, D.Q., Yang, L.X., Cao, D., Tu, W.G., Zou, Z.T., and Zou, Z.G. (2018). Role of two-dimensional nanointerfaces in enhancing the photocatalytic performance of 2D-2D MoS_2/CdS photocatalysts for H_2 production. Chem. Eng. J. *350*, 335–343.

Zhang, R., He, Y., Yi, J., Zhang, L., Shen, C., Liu, S., Liu, L., Liu, B., and Qiao, L. (2020). Proteomic and metabolic elucidation of solar-powered biomanufacturing by bio-abiotic hybrid system. Chem *6*, 234–249.

Zhukovskyi, M., Tongying, P., Yashan, H., Wang, Y.S., and Kuno, M. (2015). Efficient photocatalytic hydrogen generation from Ni nanoparticle decorated CdS nanosheets. ACS Catal. *5*, 6615–6623.

iScience, Volume *23*

Supplemental Information

Efficient Photoelectron Capture by Ni Decoration in *Methanosarcina barkeri*-CdS Biohybrids for Enhanced Photocatalytic CO_2-to-CH_4 Conversion

Jie Ye, Guoping Ren, Li Kang, Yiyun Zhang, Xing Liu, Shungui Zhou, and Zhen He

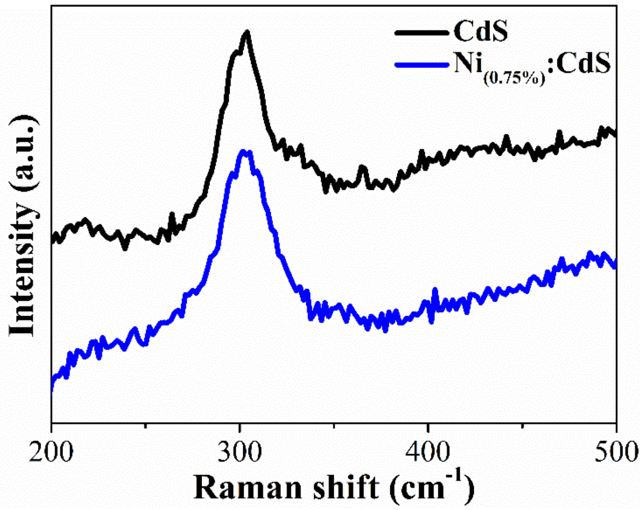

Fig. S1 The Cd-S (at 200-350 cm^{-1}) single cell Raman mapping of pure CdS and Ni$_{(0.75\%)}$:CdS nanoparticles. Related to Figure 1.

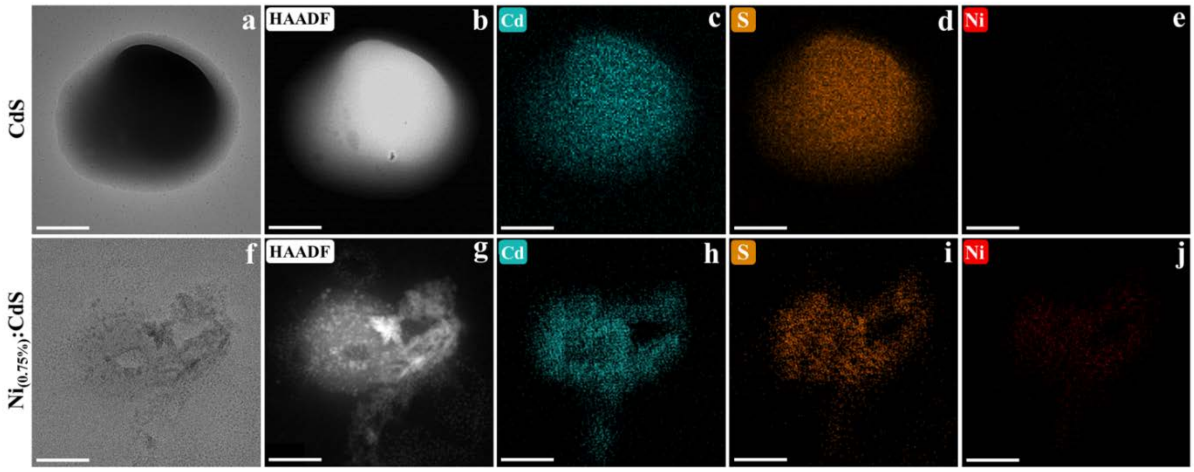

Fig. S2 TEM images (**a** and **f**), High-angle annular dark field (HAADF) images (**b** and **g**), and elements formed by Cd (**c** and **h**), S (**d** and **i**) and Ni (**e** and **j**) with EDS mapping of pure CdS and Ni$_{(0.75\%)}$:CdS semiconductors. The scale bars are 100 nm. Related to Figure 1.

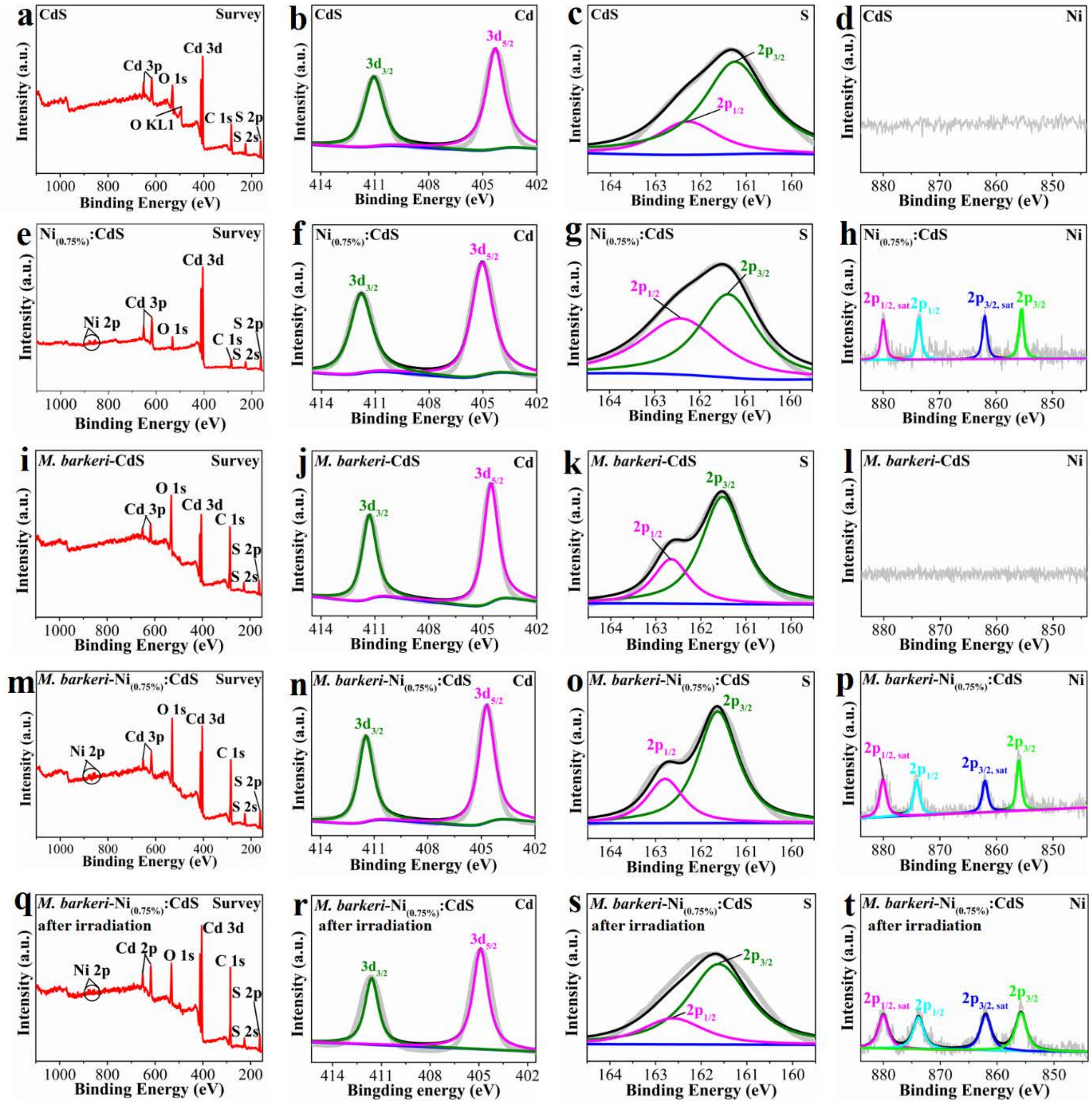

Fig. S3 XPS spectra of pure CdS semiconductor (**a**-**d**), pure $Ni_{(0.75\%)}$:CdS semiconductor (**e**-**h**), *M. barkeri*-CdS biohybrids (**i**-**l**), *M. barkeri*-$Ni_{(0.75\%)}$:CdS biohybrids (**m**-**p**) and *M. barkeri*-$Ni_{(0.75\%)}$:CdS biohybrids after irradiation (**q**-**t**). Related to Figure 1.

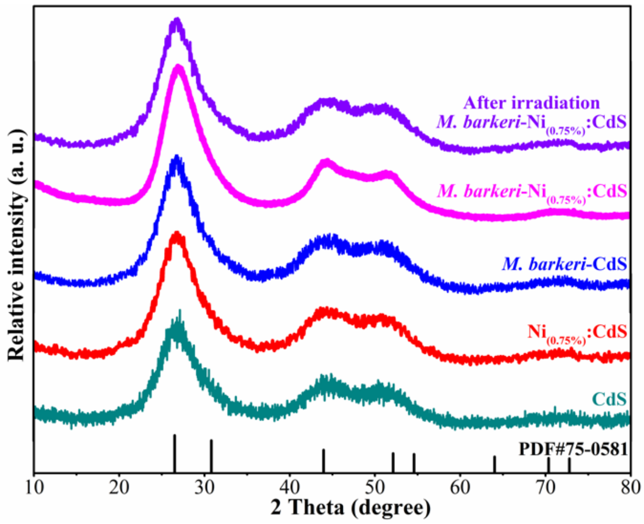

Fig. S4 X-Ray Diffraction patterns of pure CdS semiconductor, pure $Ni_{(0.75\%)}$:CdS semiconductor, *M. barkeri*-CdS biohybrids, *M. barkeri*-$Ni_{(0.75\%)}$:CdS biohybrids and *M. barkeri*-$Ni_{(0.75\%)}$:CdS biohybrids after irradiation. (reference peak from JCPDS data card No. 75-0581). Related to Figure 1.

The prepared semiconductors exhibited similar diffraction patterns, three distinct diffraction peaks at 26.7°, 44.1°, and 52.2°, which could be attributed to the (111), (220), and (311) crystal planes of CdS (JCPDS No. 75-0581), respectively. No peaks of any other impurities were detected, demonstrating the possible formation of pure CdS semiconductors. Meanwhile, The SEM and HRTEM images further indicated that almost no amorphous by-products formed during the preparation of $Ni_{(0.75\%)}$:CdS semiconductor. The fringes with d values of 0.35 nm, 0.21 nm and 0.18 nm could be attributed to the (111), (220), and (311) crystal planes of CdS, respectively.

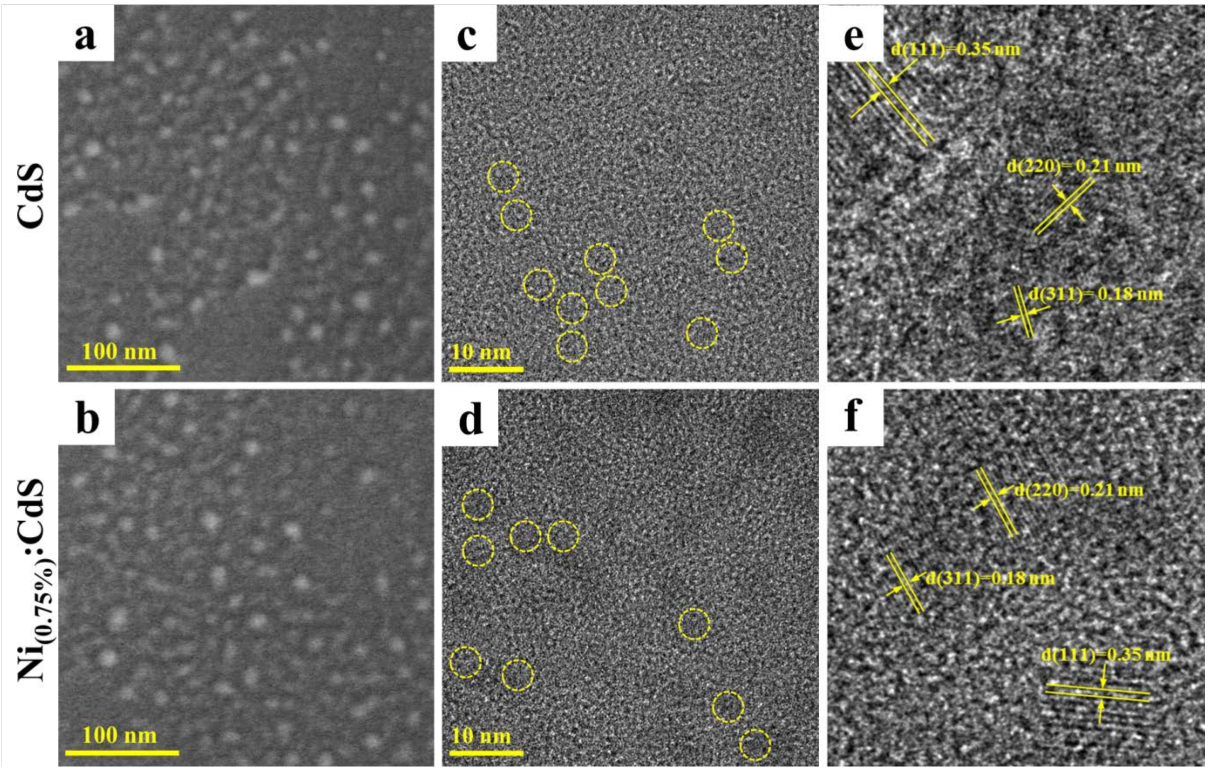

Fig. S5 The SEM images of pure CdS (**a**) and $Ni_{(0.75\%)}$:CdS (**b**) semiconductors, the high resolution TEM (HRTEM) images of pure CdS (**c**, **e**) and $Ni_{(0.75\%)}$:CdS semiconductors (**d, f**). Related to Figure 1.

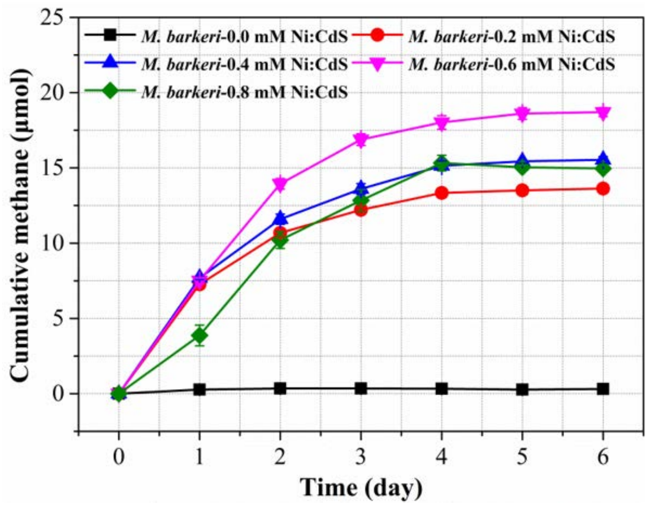

Fig. S6 Effect of different dosages on the CH_4 production performance of *M. barkeri*-$Ni_{(x)}$:CdS biohybrids. Data are represented as mean ± SEM (n = 3). Related to Figure 1.

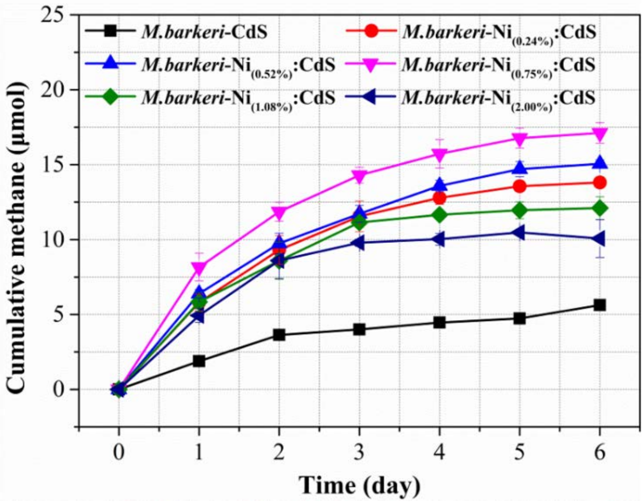

Fig. S7 Effect of different Ni weight ratios (0.24%, 0.52%, 0.75%, 1.08%, and 2.00%) on the CH_4 production performance of *M. barkeri*-$Ni_{(x)}$:CdS biohybrids. Data are represented as mean ± SEM (n = 3). Related to Figure 1.

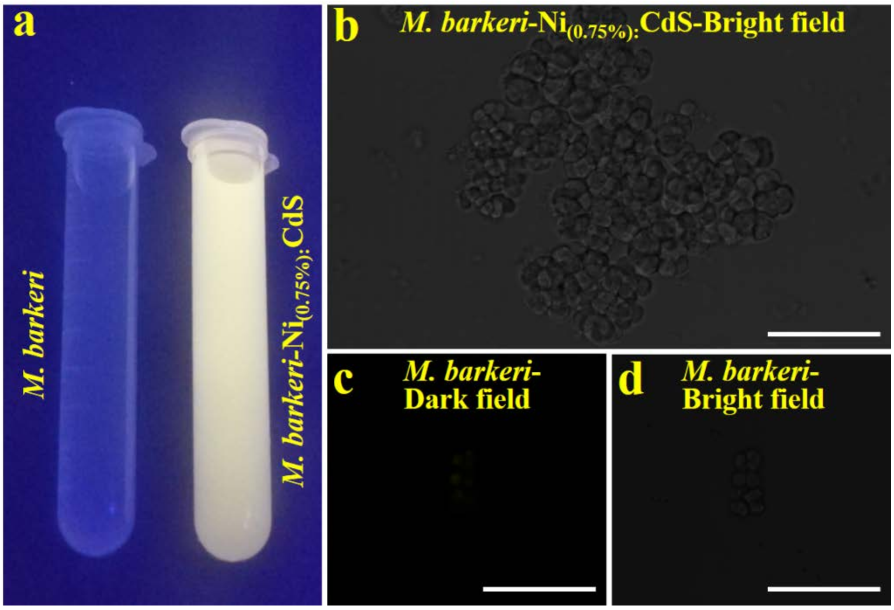

Fig. S8 Fluorescence of *M. barkeri* and *M. barkeri*-$Ni_{(0.75\%)}$:CdS under UV irradiation (a); Confocal laser-scanning microscopic image of *M. barkeri*-$Ni_{(0.75\%)}$:CdS with bright field (b); Confocal laser scanning microscopic images of *M. barkeri* with dark (c) and bright field (d) under 410 nm. All the scale bar are 20 μm. Related to Figure 1.

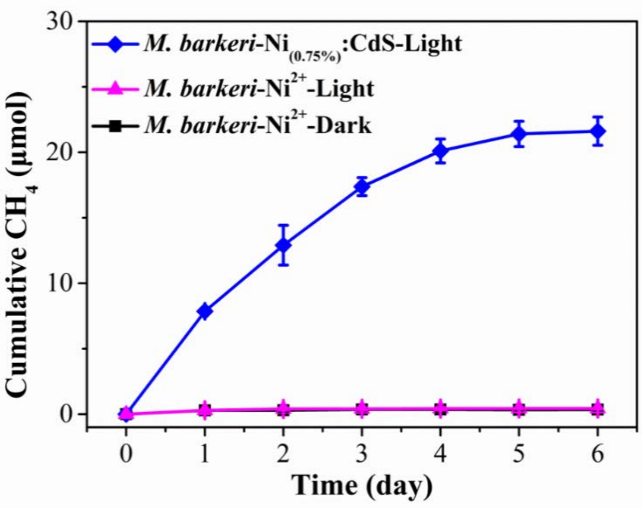

Fig. S9 The CH_4 production by *M.barkeri*-Ni^{2+}-Light and *M. barkeri*-Ni^{2+}-Dark controls with the addition of the same Ni^{2+} as that in *M. barkeri*-$Ni_{(0.75\%)}$:CdS biohybrids. Data are represented as mean ± SEM (n = 3). Related to Figure 2.

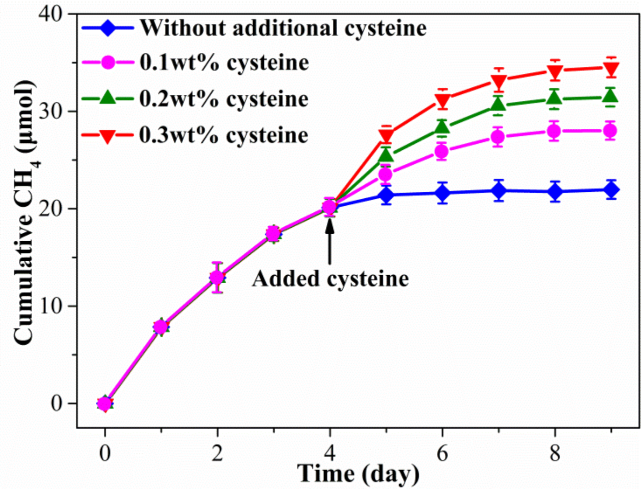

Fig. S10 Cys-dependent CH_4 yield by *M. barkeri*-$Ni_{(0.75\%)}$:CdS biohybrids with Cys added after 4 days of irradiation, for additional 5 days of photosynthesis. Data are represented as mean ± SEM (n = 3). Related to Figure 2.

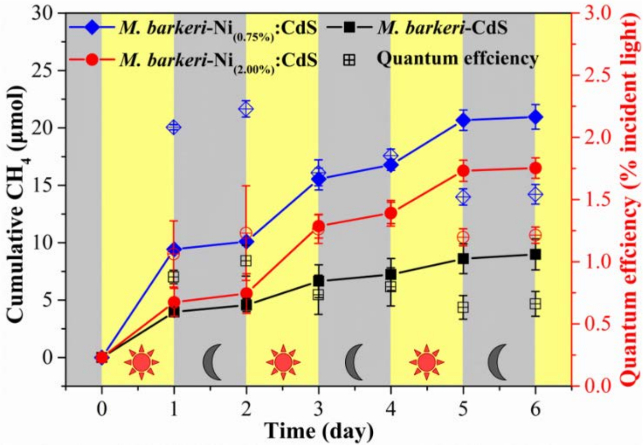

Fig. S11 Cumulative CH_4 and quantum efficiency of different biohybrids with a light-dark cycle of 1 day. Data are represented as mean ± SEM (n = 3). Related to Figure 2.

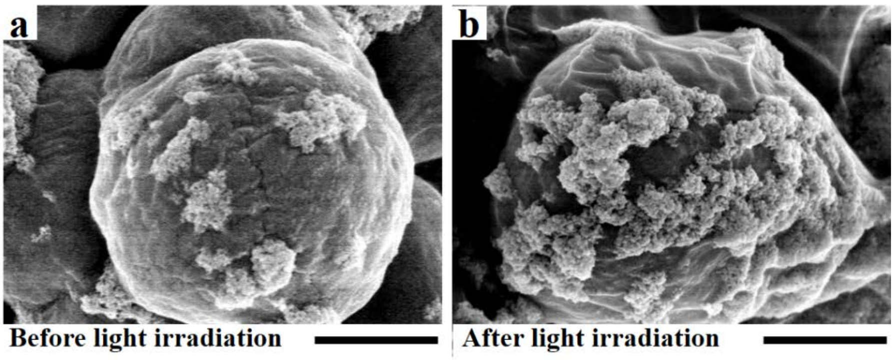

Fig. S12 SEM images of photooxidative damage to *M. barkeri*-$Ni_{(0.75\%)}$:CdS biohybrids with the light intensity of 1.6 mW/cm^2. All scale bars are 1 μm. Related to Figure 2.

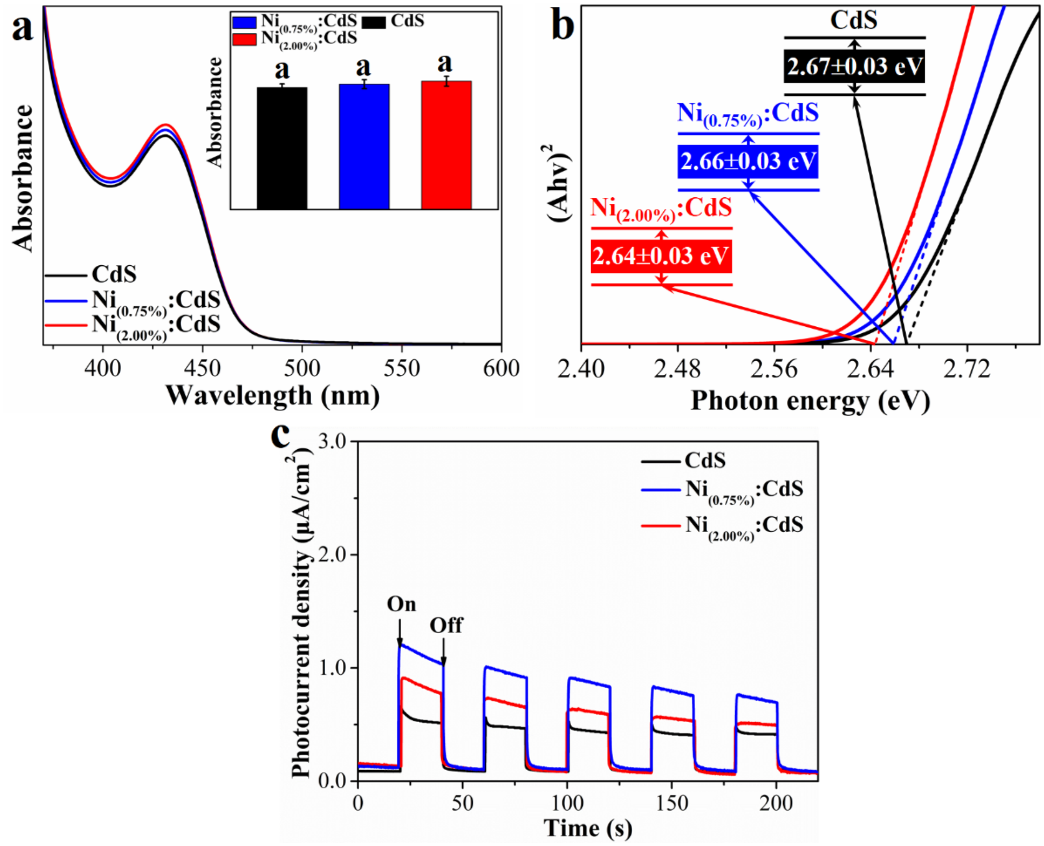

Fig. S13 UV-vis adsorption spectra (**a**), Tauc plots (**b**) and *I-t curve* (**c**) of pure CdS, $Ni_{(0.75\%)}$:CdS and $Ni_{(2.00\%)}$:CdS semiconductors. Related to Figure 3.

Although previous research demonstrated that the metal Ni might be a promising plasmonic promoter (Pei et al., 2019; Meng et al., 2014), no significant difference in the absorption intensity between CdS and $Ni_{(x)}$:CdS nanoparticles (Fig. S16), particularly in the visible light region (> 530 nm), demonstrating that no obvious plasmonic effect was performed after loading Ni atoms to CdS semiconductors. Data are represented as mean ± SEM (n = 3).

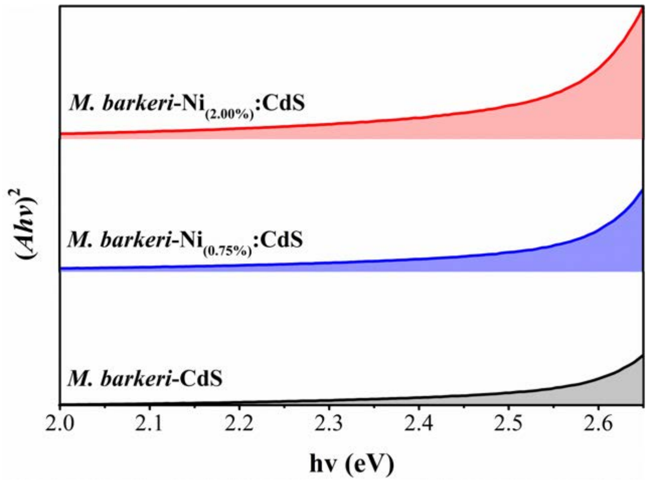

Fig. S14 Plots of $(Ahv)^2$ versus the energy of exciting light (hv) for 2.0~2.65 eV. Related to Figure 3.

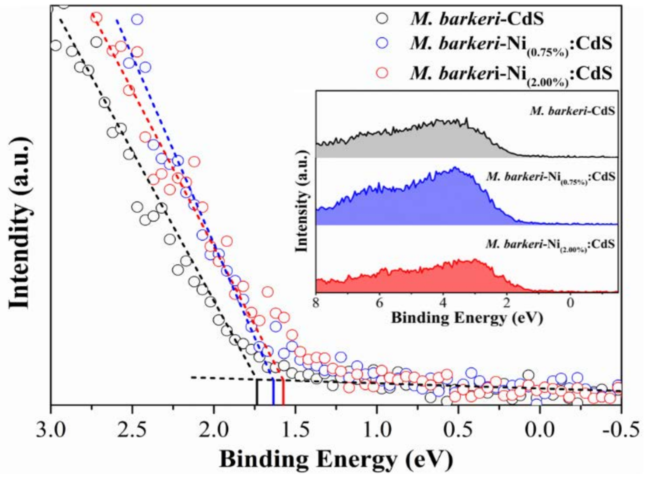

Fig. S15 Valence band XPS spectra of different biohybrids. Related to Figure 3.

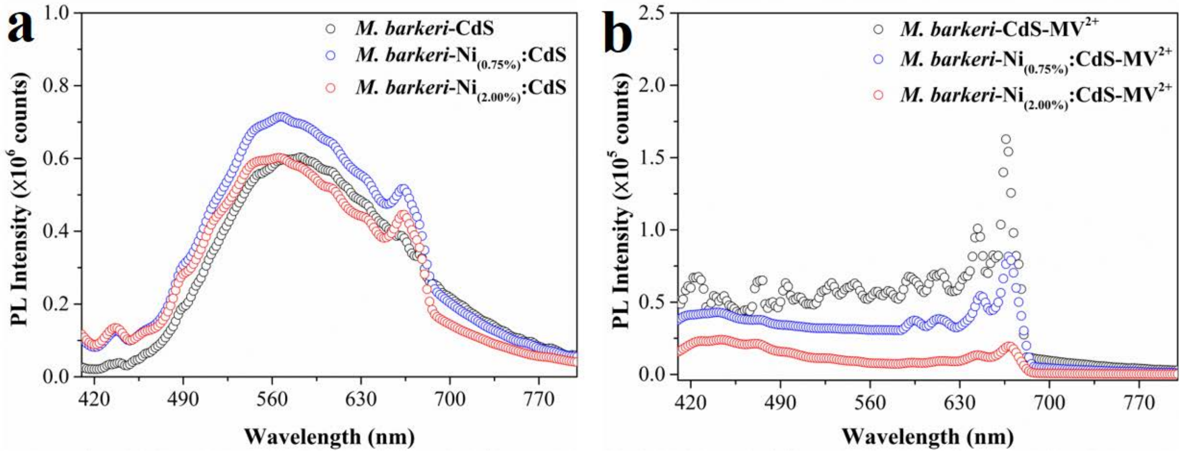

Fig. S16 PL emission spectra of three treatments in the absence (a) and presence (b) of 10^{-5} M MV^{2+} (λ_{ex} = 380 nm). Related to Figure 3.

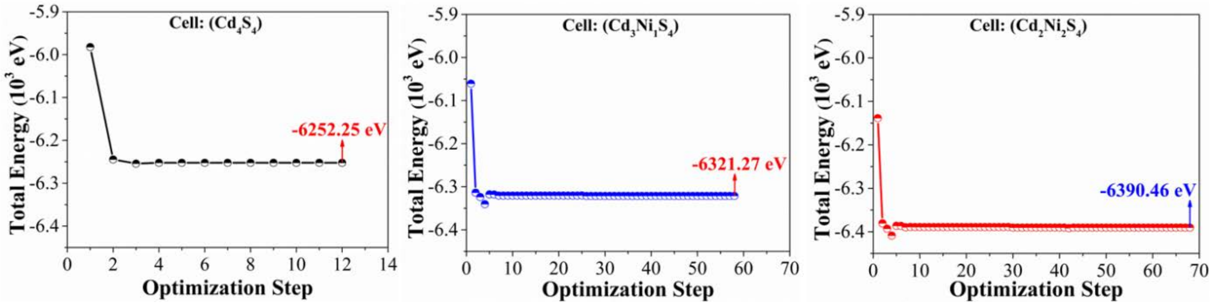

Fig. S17 Corresponding total energy evolution during geometry optimization process. Related to Figure 4.

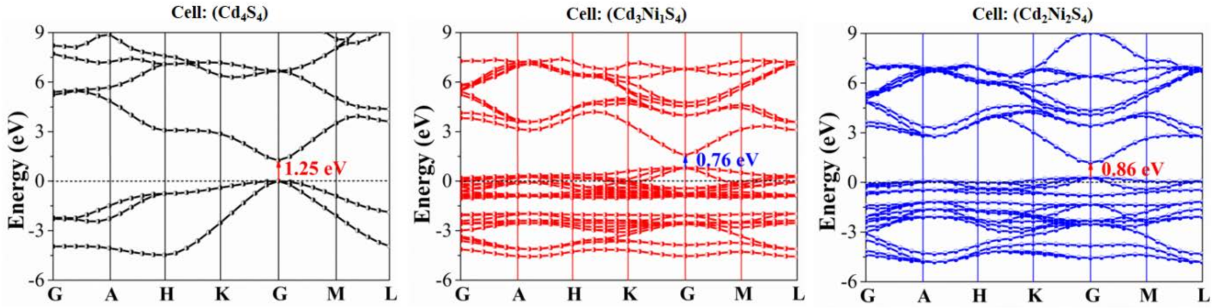

Fig. S18 Band structure plots of the simulated Ni:CdS systems. Related to Figure 4.

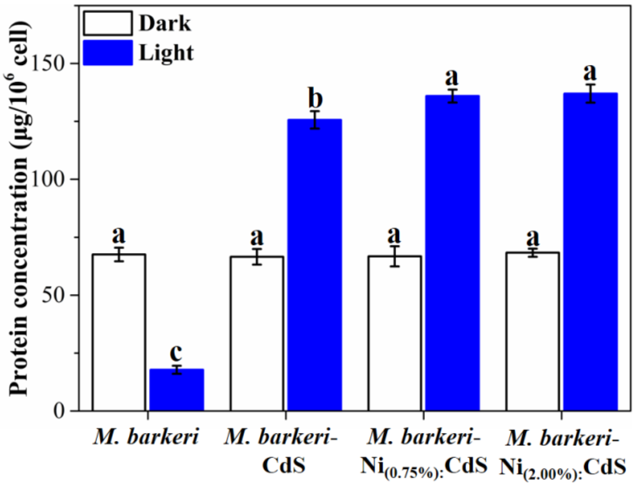

Fig. S19 Concentrations of membrane-bound protein based on the normalization results. Data are represented as mean ± SEM (n = 3), and the different letters represented statistically significant difference ($p < 0.05$) in different groups. Related to Figure 5.

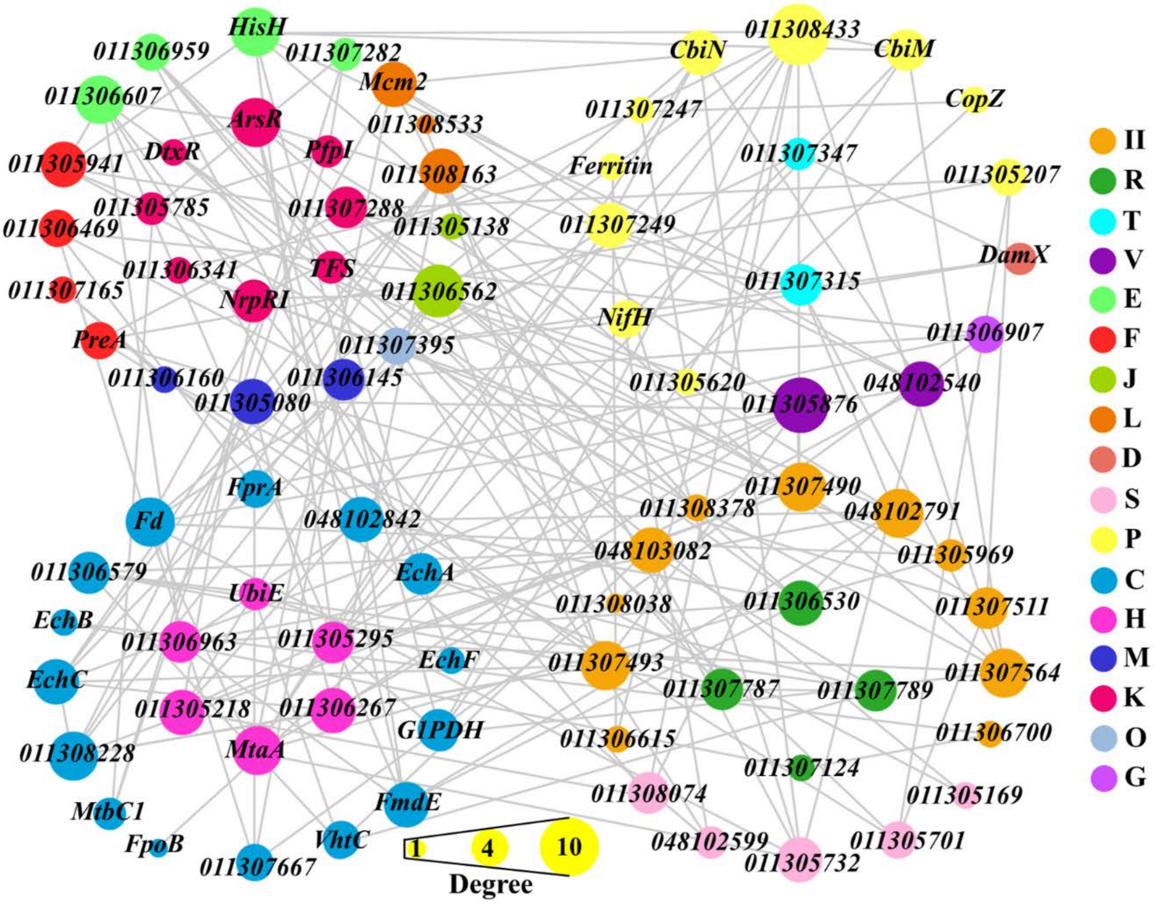

D	Cell cycle control, cell division, chromosome partitioning	**C**	Energy production and conversion
G	Carbohydrate transport and metabolism	**E**	Amino acid transport and metabolism
H	Coenzyme transport and metabolism	**F**	Nucleotide transport and metabolism
J	Translation, ribosomal structure and biogenesis	**K**	Transcription
L	Replication, recombination and repair	**R**	General function prediction only
M	Cell wall/membrane/envelope biogenesis	**S**	Function unknown
O	Posttranslational modification, protein turnover, chaperones	**T**	Signal transduction mechanisms
P	Inorganic ion transport and metabolism	**V**	Defense mechanisms
U	Intracellular trafficking, secretion, and vesicular transport	**II**	Undefinition

Fig. S20 Network analysis of the proteins with significant variations. Related to Figure 6.

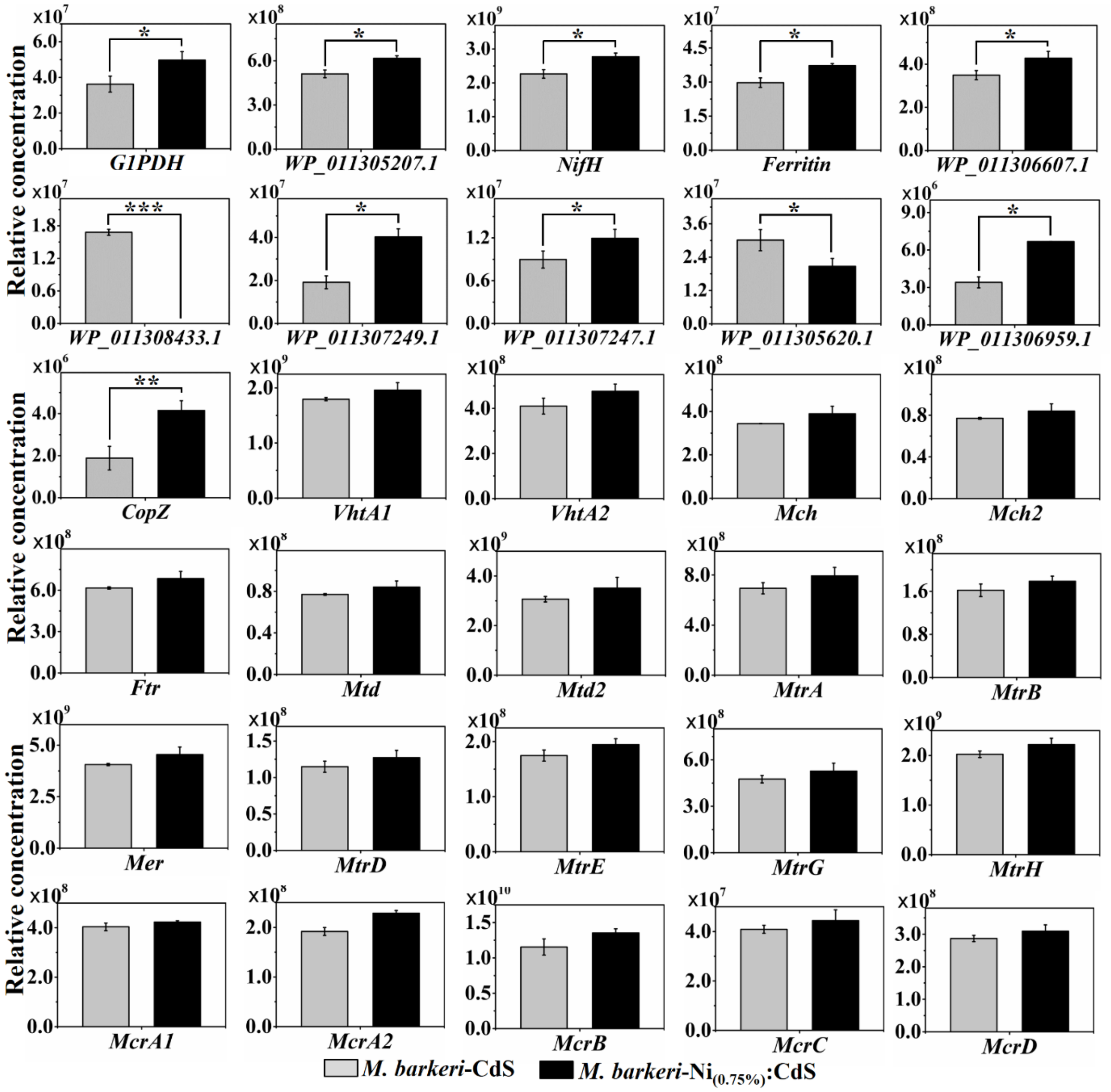

Fig. S21 Relative concentration of proteins for electron transfer, energy conversion and CO_2 fixation in *M. barkeri*-$Ni_{(0.75\%)}$:CdS biohybrids compared to *M. barkeri*-CdS biohybrids. Data are represented as mean ± SEM (n = 3). “*”, “**” and “***” indicate *p* values smaller than 0.05, 0.01 and 0.001, respectively. Three biological replicates are used. Related to Figure 7.

Table S1 The composition of contained substrate medium (CSM) and uncontained substrate medium (USM). Related to Figure 2.

Component	CSM (g/L)	USM (g/L)
$MgCl_2 \cdot 6H_2O$	0.4	0.4
$CaCl_2 \cdot 2H_2O$	0.1	0.1
NH_4Cl	0.1	0.1
KH_2PO_4	0.2	0.2
KCl	0.5	0.5
HEPES	7.16	7.16
$NaHCO_3$	2.52	2.52
$Na_2S \cdot 9H_2O$	0.24	-
NaAc	1.394	-
Cysteine-HCl	-	0.24
Trace element solution SL-10*	1 mL	1 mL
Selenite-tungastate solution**	1 mL	1 mL
Vitamin solution***	3 mL	3 mL

*Per liter, the medium containing

HCl (2M)	50 mL
$FeCl_2 \cdot 4H_2O$	2 g
$ZnCl_2$	0.2 g
$MnCl_2 \cdot 4H_2O$	0.1 g
H_3BO_3	0.18 g
$CoCl_2 \cdot 6H_2O$	0.05 g
$CuCl_2 \cdot 2H_2O$	6 mg
$NiCl_2 \cdot 6H_2O$	72 mg
$Na_2MoO_4 \cdot 2H_2O$	108 mg

**Per liter, the medium containing

NaOH	0.5 g

$Na_2SeO_3\cdot 5H_2O$	3 mg
$Na_2WO_4\cdot 2H_2O$	4 mg

***Per liter, the medium containing

4-aminobenzoic acid	0.04 g
D(+)-biotin	0.01 g
DL-a-lipoic acid	0.01 g
Calcium-D(+)-panto-thenate	0.1 g
Pyridoxine-HCl	0.1 g
Folic acid	0.03 g
Nicotinic acid	0.05 g
Riboflavin	0.05 g
Thiamin-HCl$\cdot 2H_2O$	0.01 g
Vitamin B_{12}	0.05 g

Table S2 The photocatalytic CH_4 production performance with different biohybrids. Related to Figure 2.

Biohybrid (50 mL)	*M. barkeri* inoculum (mL)	CdS (mM)	Maximum CH_4 yield* (μmol)	Average CH_4 production rate* (μmol/h)	Light intensity (mW/cm^2)	References
M. barkeri-CdS	10	1.0	13.70	0.19	1.0	Ye et al. (2019)
M. barkeri -Ni$_{(0.75\%)}$:CdS	10	0.6	21.50	0.21	0.8	In this study
M. barkeri -Ni$_{(0.75\%)}$:CdS	10	0.6	23.04	0.24	1.0	In this study

* The value was calculated with the data that were statistically significant.

Table S3 Fit parameters for the PL decay curves of *M. barkeri*-Ni$_{(x)}$:CdS. Related to Figure 3.

	A_1	A_2	τ_1 (ns)	τ_2 (ns)	τ (ns)
M. barkeri-CdS	336.95	16.09	0.32	3.45	1.38
M. barkeri-Ni$_{(0.75\%)}$:CdS	423.16	64.24	0.80	7.00	4.32
M. barkeri-Ni$_{(2.00\%)}$:CdS	496.00	17.57	0.38	7.20	3.14

Based on the PL decay curves (Figure 3d), the parameters in Table S2 can be obtained through curve fitting. The average lifetime of the QD PL decay is calculated by using following expression:

$$\tau = \frac{\sum_n (A_n \tau_n{}^2)}{\sum_n A_n \tau_n}$$

where n corresponds to the nth component of a given multi-exponential decay process (James et al., 1985).

Materials and methods

Synthesis of Ni:CdS semiconductors

The synthesis of Ni:CdS semiconductors were conducted according to the previous research (Wang et al., 2018), where 3-Mercaptopropionic acid (MPA) was used to disperse and control the particle size of CdS nanoparticles. Briefly, 5 mmol of $CdCl_2$ and 8.5 mmol of MPA were added into 100 mL of water. In addition, the Ni amount (wt. %) was varied to control the dosage volume of $NiCl_2$ to construct $Ni_{(x)}$:CdS semiconductors, where x is the nominal loading amount of Ni, which is determined by the ICP-MS measurement. For example, the addition of 10 μmol of $NiCl_2 \cdot 6H_2O$ produced 65.3 ± 0.5 mg of $Ni_{(0.75\%)}$:CdS semiconductors. Before transferring the solution into a 250 mL three-necked flask, the pH was adjusted to 10.0 by 5.0 mol/L of NaOH solution. Then, the air in the headspace of the flask was replaced with Ar, and 0.5 mmol of freshly prepared Na_2S solution was dropwise added under stirring. Subsequently, the mixture was heated to 100 ^{o}C with a condenser, and the observed bright-yellow, transparent solution was continually stirred at 100 ^{o}C for 30 min. After natural cooling to room temperature, the $Ni_{(x)}$:CdS semiconductors were isolated through precipitation with alcohol. Then, the pellet was redispersed in water and freeze dried for further use. As control, CdS semiconductors with the identical particle size were synthesized by the same method without Ni. All analytical-grade chemicals were purchased from Sigma-Aldrich and used without further purification.

Construction and characterization of *M. barkeri*-Ni:CdS biohybrid

The inoculum of *M. barkeri* (DSM 800, obtained from DSMZ, Braunschweig, Germany) was cultured in a 50-mL anaerobic heterotrophic medium at 37 ^{o}C (Table S1). When the growth of

M. barkeri reached an exponential phase (OD_{600}~0.2), 0.6 mmol/L $Ni_{(x)}$:CdS semiconductors were added according to the preliminary experiment, and the mixture was placed in the shaker at a speed of 180 rpm to create an *M. barkeri*-$Ni_{(x)}$:CdS biohybrid. After 3 days of cultivation, the suspension was sequentially centrifuged, washed, and resuspended in 5 mL 0.9% NaCl solution three times. As control, the *M. barkeri*-CdS biohybrid was prepared by the same method, except $Ni_{(x)}$:CdS was replaced with CdS semiconductors.

The prepared *M. barkeri*-$Ni_{(x)}$:CdS/*M. barkeri*-CdS biohybrids were collected, fixed by 4% glutaraldehyde, and sequentially dehydrated to prepare nonsectioned and thin-sectioned samples (Wang et al., 2019). Fluorescence images were collected using a Carl Zeiss LSM880 confocal laser-scanning microscope (CLSM). Micro-Raman measurement was performed using a Renishaw micro-Raman spectrometer (Tian et al., 2019). The high-resolution/transmission electron microscopy (HR-/TEM) images were obtained with a FEI Tecnai G2 F20 S-TWIN field-emission transmission electron microscope. Elemental mapping was performed by an X-MaxN energy dispersive X-ray spectrometer (EDS) attached to the TEM instrument. The X-ray diffraction (XRD) patterns were recorded with a Shimadzu XRD-6000 X-ray diffractometer. The X-ray photoelectron spectroscopy (XPS) and valence band XPS (VB XPS) experiments were conducted by a Thermo ESCALAB 250XI XPS spectrometer system.

A CHI 660E electrochemical workstation (CH Instruments Inc, Austin, TX) was used for the electrochemical measurements with 395 ± 5 nm violet LED irradiation (1.0 mW/cm^2) in a three-electrode system under N_2 gas atmosphere according to the previous research (Ye et al., 2018; Ye et al., 2019). A platinum sheet and a saturated calomel electrode (SCE) were used as the contour and reference electrodes, respectively. The thin-film working electrodes were prepared by drop-casting 50 μL of suspensions (3 mg of semiconductors/biohybrids after dispersed in 0.5 mL of 1:3 v/v isopropyl alcohol/water solvent) onto indium tin oxide (ITO) glass substrates (1×1 cm), followed by drying the film overnight. A 100 mM phosphate buffer solution (PBS) (pH = 7) was used as the electrolyte solution (prepared with 0.13 g/L KCl, 5.93 g/L $NaH_2PO_4 \cdot 2H_2O$ and 22.2 g/L $Na_2HPO_4 \cdot 12H_2O$). The photocurrent (I-t) was measured by light irradiation (light on/off cycles: 20 s) at a bias potential of -0.4 V (vs. SCE). The square wave voltammetry (SWV) between -0.6 and 0 V (vs. SHE) was performed with a scan rate of 2 mV/s. The electrochemical impedance spectroscopy (EIS) analyses were conducted in a frequency range of 1×10^5 to 0.1 Hz with a sinusoidal perturbation amplitude of 5 mV. Linear sweep voltammetry (LSV) was operated from 0.3 to -1.5 V (vs. SCE) with a scan rate of 2 mV/s in an aqueous solution. A glassy carbon electrode (3 mm in diameter) was used as the working electrode, and the samples were loaded by transferring the catalyst dispersion (3 mg of biohybrids, 50 μL of 5 wt% Nafion solution, and 1.0 mL of ethanol solvent) onto the glassy carbon, followed by drying the film overnight. Steady-state photoluminescence (PL) spectra and PL decay spectra were determined on the FLS980 photoluminescence spectrometer. The lifetime data were analyzed with DataStation V6.6 (Horiba Scientific). The ultraviolet/visible (UV-vis) diffused reflectance spectra and UV-vis absorption spectra were recorded on a Shimadzu UV2600 UV spectrometer.

As indicative of biomass growth, the total protein content of *M. barkeri* was analyzed following a previously reported method (Pushpakumari Kudahettige et al., 2018). Membrane-bound proteins of *M. barkeri* were mechanically isolated as described (Mehta et al., 2005), and measured with the BCA Protein Assay Kit (Thermo Scientific Pierce). The concentrations of

Cd and Ni elements in the membrane-bound protein of *M. barkeri* were quantified with a NexION 300X inductively coupled plasma mass spectrometer. The NADH/NAD ratio of *M. barkeri* was measured with the Sigma-Aldrich NADH/NAD quantification kit (MAK 037). The number of cells in different samples was measured by flow cytometry (Quanta SC, Beckman Coulter) according to Xiao et al. (2017).

Photocatalytic CO_2-to-CH_4 conversion experiments

The photocatalytic CO_2-to-CH_4 conversion experiments were conducted in 125-mL serum bottles with 50-mL sterilized autotrophic medium (pH = 6.8, Table S1). After flushing the bottles with CO_2:N_2 (80:20) for 30 min, 5 mL *M. barkeri*-$Ni_{(x)}$:CdS suspension and cysteine at 0.15 wt% (sacrificial agent) were added. Then, the bottles were placed in a constant temperature incubator to maintain at 35 ± 2 °C, and irradiated by a visible-light source. The 395 ± 5 nm violet LEDs and 300 W Xenon lamp (CEL-HXF300, Ceaulight, China) with a 400 nm filter were employed as the visible-light source. Parallel studies were conducted, Where *M. barkeri*, $Ni_{(x)}$:CdS, and light were removed or replaced by CdS semiconductors, while 0.15 wt% cysteine was still added. The CH_4 concentration was determined by a Shimadzu GC2014 gas chromatograph. Moreover, the isotope-labeled experiments were conducted using $NaH^{13}CO_3$ instead of $NaH^{12}CO_3$ in the medium. Then, the products were measured with an Agilent 7890-5975c gas chromatography-mass spectrometer (GC-MS). The average quantum yield (*QE*) was calculated according to previous research (Sakimoto et al., 2016). The photosynthetic CH_4 efficiencies of *M. barkeri*-$Ni_{(0.75\%)}$:CdS biohybrids could also be calculated based on the initial Cys concentration according to Eq. S1. The 0.15 wt% Cys·HCl (MW = 157.62 $g \cdot mol^{-1}$) in the photosynthesis measurements, corresponds to 457.83 μmol Cys. With the above stoichiometry, this leads to a maximum CH_4 production yield of 57.23 μmol. Then the quantum yield based on the initial Cys concentration is defined as:

$$\text{Quantum yield}(\%) = \frac{n_{CH_4}}{57.23} \times 100\% \qquad \text{(S1)}$$

where n_{CH_4} is the CH_4 yield.

Density functional theory (DFT) theoretical calculation

Three greenockite models were established with different numbers of Ni atoms in the 8 atom cells, which are named Cd_4S_4, $Cd_3Ni_1S_4$, and $Cd_2Ni_2S_4$. Their electronic structures were investigated via the plane-wave-pseudopotential approach based on the density functional theory. For the original model, we determined the stability of the doped structure before calculating the electronic structures. The convergence tolerances for the energy, maximum force, maximum stress, maximum displacement were set to 5.0×10^{-6} eV/atom, 0.01 eV/Å, 0.02 GPa, 5.0×10^{-4} Å, respectively. The electronic exchange-correlation energy was calculated with Perdew-Burke-Ernzerhof (PBE) of the generalized gradient approximation. The electron-core interaction was using norm conserving pseudopotentials with a plane-wave basis cutoff energy of 290 eV. The self-consistent field tolerance was 5.0×10^{-6} eV/atom. The FFT grids and augmentation density scaling factor of all models were 36×36×36 and 1.5, respectively. The k-points were set to 4×4×4 for all optimized models.

References

James, D. R., Liu, Y. S., Mayo, P. De, Ware, W. R. (1985). Distributions of fluorescence lifetimes: consequences for the photophysics of molecules adsorbed on surfaces. *Chem. Phys. Lett. 120*, 460-465.

Mehta, T., Coppi, M. V., Childers, S. E., Lovley. D. R. (2005). Outer membrane c-type cytochromes required for Fe (III) and Mn (IV) oxide reduction in *Geobacter sulfurreducens*. Appl. Environ. Microbiol. *71*, 8634-8641.

Meng, X., Wang, T., Liu, L., Ouyang, S., Li, P., Hu, H., Kako, T., Iwai, H., Tanaka, A., Ye, J. (2014). Photothermal conversion of CO_2 into CH_4 with H_2 over Group VIII nanocatalysts: an alternative approach for solar fuel production. Angew. Chem. Int. Edit. *53*, 11478-11482.

Pei, L., Li, T., Yuan, Y., Yang, T., Zhong, J., Ji, Z., Yan, S., Zou, Z. (2019). Schottky junction effect enhanced plasmonic photocatalysis by TaON@ Ni NP heterostructures. Chem. Commun. *55*, 11754-11757.

Pushpakumari Kudahettige, N., Pickova, J., Gentili, F. G. (2018). Stressing algae for biofuel production: Biomass and biochemical composition of *Scenedesmus dimorphus* and *Selenastrum minutum* grown in municipal untreated wastewater. Front. Energ. Res. *6*, 132.

Sakimoto, K. K., Wong, A. B., Yang, P. (2016). Self-photosensitization of nonphotosynthetic bacteria for solar-to-chemical production. Science *351*, 74-77.

Tian, L. J., Min, Y., Li, W. W., Chen, J. J., Zhou, N. Q., Zhu, T. T., Li, D. B., Ma, J. Y., An, P. F., Zheng, L. R., Huang, H., Liu, Y. Z., Yu, H. Q. (2019). Substrate metabolism-driven assembly of high-quality CdS_xSe_{1-x} quantum dots in *Escherichia coli*: Molecular mechanisms and bioimaging application. ACS Nano *13*, 5841-5851.

Wang, B., Xiao, K., Jiang, Z., Wang, J., Jimmy, C. Y., Wong, P. K. (2019). Biohybrid photoheterotrophic metabolism for significant enhancement of biological nitrogen fixation in pure microbial cultures. Energ. Environ. Sci. *12*, 2185-2191.

Wang, J., Xia, T., Wang, L., Zheng, X. S., Qi, Z. M., Gao, C., Zhu, J. F., Li, Z. Q., Xu, H. X., Xiong, Y. J. (2018). Enabling visible−light−driven selective CO_2 reduction by doping quantum dots: Trapping electrons and suppressing H_2 evolution. Angew. Chem. Int. Edit. *57*, 16447-16451.

Xiao, Y., Zhang, E., Zhang, J., Dai, Y., Yang, Z., Christensen, H. E., Ulstrup, J., Zhao, F. (2017). Extracellular polymeric substances are transient media for microbial extracellular electron transfer. Sci. Adv. *3*, e1700623.

Ye, J., Hu, A. D., Ren, G. P., Chen, M., Tang, J. H., Zhang, P. Y., Zhou, S. G., He, Z. (2018). Enhancing sludge methanogenesis with improved redox activity of extracellular polymeric substances by hematite in red mud. Water Res. *134*, 54-62.

Ye, J., Yu, J., Zhang, Y. Y., Chen, M., Liu, X., Zhou, S., He, Z. (2019). Light-driven carbon dioxide reduction to methane by *Methanosarcina barkeri*-CdS biohybrid. Appl. Catal. B-Environ. *257*, 117916.